Atmospheric Turbulence Measurements at a Coastal Zone with and without Fog

Andrey A. Grachev[1,2,3,*] • Raghavendra Krishnamurthy[3,4] • Harindra J. S. Fernando[3] • Christopher W. Fairall[1] • Stef L. Bardoel[3] • Sen Wang[3]

Received: 5 July 2020/ Accepted: 25 July 2021/ Published online: DD Month YEAR

Abstract

Measurements of atmospheric turbulence at a site in Ferryland (Newfoundland) during the C-FOG (Coastal-Fog) field campaign in September–October 2018 are used to study meteorological parameters, turbulent statistics, internal boundary layers, and scaling laws for turbulent mixing in the coastal zone. We observe stable/unstable shallow internal boundary layers with a region of unstable/stable stratification above with onshore flow from a relatively warm/cold sea onto the cold/heated land during the night/day. This study compares surface fluxes and other turbulence statistics as well as different scaling laws with and without fog. While both complexity of the coastal landforms and foggy conditions nominally violate assumptions underlying Monin–Obukhov similarity theory (MOST), our observations show that the non-dimensional standard deviations of the wind components and the dissipation rate of turbulence kinetic energy obey MOST reasonably well for all measurement levels, stability condition, and wind direction for both fog and no fog cases. However, the data scatter for the normalized dissipation rate is somewhat greater compared with the normalized standard deviations of the wind components. The bias and relatively larger scatter of normalized standard deviations for scalars in near-neutral conditions is

✉ Andrey A. Grachev
Andrey.Grachev@colorado.edu

[1] NOAA Physical Sciences Laboratory, Boulder, CO, USA

[2] Cooperative Institute for Research in Environmental Sciences, University of Colorado, Boulder, CO, USA

[3] Department of Civil & Environmental Engineering & Earth Sciences, Department of Aerospace and Mechanical Engineering, University of Notre Dame, Notre Dame, IN, USA

[4] Pacific Northwest National Laboratory, Richland, WA, USA

[*] Currently at: Boundary Layer Research Team/Atmospheric Dynamics & Analytics Branch, DEVCOM Army Research Laboratory, White Sands, NM, USA

likely associated with the underlying inhomogeneous coastal surface. According to the C-FOG data, during a fog event the moisture flux data can become irregular and the latent heat flux is often negative (downward). Our observations also demonstrate a poor agreement between normalized standard deviations of specific humidity with MOST for foggy conditions; its statistical dependence on the MOST stability parameter was weak at best in fog.

Keywords Air–Sea/Land Interaction · Coastal Fog · Coastal Zone · Internal boundary layer · Monin–Obukhov similarity theory

1 Introduction

Quantification of the momentum, heat, and mass exchanges between the atmosphere and underlying surface and small-scale turbulence is a central problem in atmospheric boundary-layer (ABL) research. Turbulence measurements in a coastal zone (considered in this study) can provide valuable information on statistics needed for energy and mass exchange, modelling of air pollution dispersion, estimation of wind loads on structures, and other important applications in a coastal-zone environment. Furthermore, it is also important to have a good assessment of wind speed and turbulence profiles for offshore wind farms that play a significant role in renewable energy (e.g., Emeis 2014). It should be noted that evaluation of traditional flux-profile relationships, usually described by classical Monin–Obukhov similarity theory (MOST), in a coastal zone is complicated because assumption of horizontal homogeneity underlying MOST in the case of heterogeneous terrain is not always met. However, study of the coastal zone and its adjacent areas on- and offshore is important for many reasons.

The coastal zone can be defined as the transitional area where marine and terrestrial environments influence each other (e.g., Carter 1988). For example, a sea-breeze front penetrates inland for distances of tens of kilometres (up to 100 km and even further). Frequently, the coastal zone is just identified as a zone within about 100 km inland or offshore of a coastline. However, we consider only a part of the coastal zone, the relatively narrow strip of land and sea areas bordering the shoreline, which are influenced by the coastal processes. The problem of air–sea/land interaction in a coastal zone with a focus on small-scale turbulent processes has been widely investigated in many studies (e.g., Mahrt et al. 1998, 2016; Sun et al. 2001; Geernaert 2002; Ortiz-Suslow et al. 2015, 2018; Grachev et al. 2018a, and references therein). Here, we analyze and discuss measurements of atmospheric turbulence at a coastal zone with and without fog. Coastal marine fog is an important meteorological phenomenon that has significant adverse impacts in a coastal zone including ground and air transportation as well as the propagation of electromagnetic waves in the atmosphere, including wave ducting. For example, the relatively cold ocean waters off California lead to year-round fog formation, which penetrates to a variable yet relatively consistent extent inland causing traffic disorder, fog-delayed flights, etc. due to low visibility in dense fog (Torregrosa et al. 2014).

There is a long history of studying the formation, evolution, and dissipation of marine fog, and the literature on the subject is vast. A review of marine-fog research in light of achievements, recent advances, and future perspectives can be found in Wang (1985), Lewis et al. (2004), Gultepe et al. (2007; 2009), Koračin et al. (2014), Koračin and Dorman (2017). These review papers also discuss and summarize observations, development of forecasting models, and remote-sensing methods for fog-related research in detail. In spite of the myriad of studies devoted to fog research, the challenges of forecasting/nowcasting persist because of considerable time and space variability within fog caused by interactions among various processes (Gultepe et al. 2007, 2009, 2017).

Formally, fog forms when humid air becomes saturated and water vapour condensation occurs by either cooling air to its dew point (temperature decreases) or by adding enough moisture to reach saturation (dew point increases). Fog, mist, and haze are the terms generally used to describe low visibility due to water droplets, ice crystals, and/or dry particles suspended in the air (e.g., Gultepe et al. 2007, 2017). Fog reduces visibility to less than 1 km (the international definition of fog), mist has visibility of between 1 km and 2 km, and haze reduces visibility to between 2 km and 5 km (e.g., Vautard et al. 2009). Fog and mist are generally assumed to be composed of droplets that are principally water. Haze (and smoke) is a significantly different phenomenon caused by the suspension of extremely small particles in the air and it is directly related to air pollution. Nonetheless these terms are sometimes used loosely in the literature. According to the International Civil Aviation Organization present weather code (ICAO 2007), mist is defined as a visibility of between 1 km and 5 km. Based on the data collected during the C-FOG (Coastal-Fog) field campaign, Dorman et al. (2021) found that "1–6 km visibility is a good marker of near-fog conditions due to water droplets", which can be considered as the range of mist visibility. Thus, Dorman et al. (2021) suggested a visibility threshold of 1 km for fog and an upper visibility threshold of 6 km for mist (i.e., mist is a visibility of between 1 km and 6 km). We also adhere to this definition of fog and mist here.

There are many different types of fog, such as advection fog, radiation fog, steam (evaporation) fog, valley fog, upslope fog, precipitation fog, freezing fog, and ice fog among others. Gultepe et al. (2007) analyzed eleven types of fog based on previously established classifications. Fog is generally classified into different types, depending on how it forms (i.e., according to the physical process, chemical composition, etc.), although, fog occurrences often involve multiple processes. A review of approaches used in the classification of fog can be found in Gultepe et al. (2007, 2009, 2017). Marine fog, a phenomenon occurring at both coastal and open ocean areas, is usually the result of advection of warm air masses over cold sea surfaces (cold sea fog) or colder air flowing over a warmer sea (warm sea fog) (e.g., Koračin et al. 2014; Gultepe et al. 2017). Another common type of marine fog is evaporation-mixing fog (also referred to as steam fog or sea smoke), which occurs when evaporation takes place into air that is much colder than the water surface. This type of fog is observed for both strong and light winds in the case of free convection (Saunders 1964; Golitsyn and Grachev 1986; Koračin et al. 2014). Steam fog is frequently observed over lakes in wintertime and over polynyas and leads in the Arctic.

Improvement of marine fog-forecasting requires, in particular, better understanding the role of small-scale turbulence in fog (Lewis et al. 2004; Koračin et al. 2014; Kim and Yum 2017). Note that eddy diffusion is the key mechanism in advection and steam fog. However, direct measurements of atmospheric turbulence in marine fog are difficult and there are only a few works on this subject. Fairall et al. (1977) analyzed the dissipation rate of turbulence kinetic energy, ε, and temperature structure function, C_T^2, measured in the marine boundary layer off the southern California coast. According to Fairall et al. (1977), an ensemble average of the fog events showed that ε and C_T^2 reach peak values immediately before and after the fog is encountered.

Application of the version 3.0 of the Coupled Ocean-Atmosphere Response Experiment (COARE) bulk algorithm (Fairall et al. 2003) over coastal shoaling waters of the Atlantic Ocean south of Martha's Vineyard, Massachusetts, was examined by Edson et al. (2007) to investigate influences of fog on the fluxes measured from the Air-Sea Interaction Tower (ASIT) during intensive operating periods of the Coupled Boundary Layer Air-Sea Transfer Experiment for Low to Moderate Winds (CBLAST-LOW). In particular, they reported a negative latent heat flux (downward moisture flux) during a case study of an eight-day period characterized by light winds, a stably stratified ABL, and swell-dominated waves. According to the CBLAST-LOW data, the drag coefficient shows good agreement in the mean with the COARE 3.0 algorithm. However, Dalton numbers computed in stable conditions observed at the ASIT are substantially lower than the standard COARE 3.0 parametrization derived for open ocean conditions.

Downward (negative) fluxes of moisture in the ABL under foggy conditions were also reported by Heo et al. (2010) and Huang et al (2015). Heo et al. (2010) analyzed advection and steam fog cases over the sea using the data collected at a tower situated on submarine rock, where the Yellow Sea intersects with the East China Sea. According to Heo et al. (2010), extreme values of the negative latent heat of ≈ –200 Wm^{-2} (Heo et al. 2010, Fig. 4a, b) and ≈ –300 Wm^{-2} (Heo et al. 2010, Fig. 9a, b) for advection and steam fogs, respectively, were observed prior to the fog formation, which is apparently due to condensation in the stable surface layer. Huang et al. (2015) focused on small-scale turbulence, boundary-layer structure, and synoptic information based on measurements made from a coastal offshore platform in the South China Sea. The results for warm air advection fogs over the South China Sea were similar to Edson et al. (2007) (mostly between 0 and –30 Wm^{-2}), while Heo et al. (2010) observed generally larger values.

Available limited observations of atmospheric turbulence in the presence of fog still remain a challenge for the validation and calibration of coastal fog forecasting models. The C-FOG (Coastal Fog) field program dealt with field measurements on the continental shelf of the eastern Canadian Atlantic during September–October 2018 using a research vessel, covering either side of the air–water interface as well as measurements at two coastal supersites in Nova Scotia and Newfoundland (Fernando et al. 2021). The region is rich in marine fog, and conducive to disparate types of fog (Dorman et al. 2017, 2020). The cool Labrador Current meets the warm Gulf Stream at the Grand Banks south-east of Newfoundland. The combination of these two currents produces heavy fogs. This region also is known as "Iceberg Alley", one of the world's most dangerous shipping areas. Note that Newfoundland is one of the worlds' two sites of greatest marine fog occurrence based on ship weather measurements (Dorman et al. 2017, 2020). Here we report some results of turbulent measurements from the C-FOG field campaign carried out near the town of Ferryland on the Avalon Peninsula, Newfoundland, Canada (south of the city of St. John's).

The main objectives of this study are twofold. The first is an investigation of the coastal air–sea/land coupling in an area of complex terrain off Eastern Canada along the coast of Newfoundland. In some sense, this study is in part based on our previous results on the effects of coastal processes on momentum, mass, and heat exchange in the coastal zone of the Outer Banks near the town of Duck, North Carolina during the Coupled Air-Sea Processes and EM Ducting

Research (CASPER) field campaign in October–November 2015 (Grachev et al. 2018a; Wang et al. 2018). The second is to advance understanding of turbulence properties during marine fog events in the coastal zone, thus providing modellers with a database on turbulence in coastal fog-laden air.

2 The C-FOG Ferryland Observation Site and Instrumentation

As mentioned, this study uses atmospheric turbulence data collected at a supersite located near a small seaside fishing town called Ferryland (on the Island of Newfoundland) during the C-FOG field campaign. General information about the C-FOG program and the field experiments can be found in the review article by Fernando et al. (2021) and in a series of specific studies by Bardoel et al. (2021), Dorman et al. (2021), Gultepe et al. (2021), Perelet et al. (2021) and others in this special issue. The town of Ferryland is located approximately 80 km south of St. John's on the south-eastern coast of the Avalon Peninsula exposed to the north-west Atlantic where large storms frequently affect coastal zones. This region was chosen because of the convenience for experimental operations and extensive fog development potential based on climatology (Dorman et al. 2017). The topography of the area is complex, with high rock cliffs, islands, tombolo, rocky shoreline, valleys, and other features including inlets and bays. The weather and fog formation along the coast of the eastern Avalon is changeable and difficult to forecast due to variability caused by the complex topography.

Figure 1 shows the study area located on a long peninsula just east to Ferryland. The peninsula encompasses two main landforms (or a tombolo cluster a.k.a. tied islands) referred to locally as "The Downs" and "Ferryland Head". The Downs is a rising ground mainly devoid of trees and connected to the mainland (Ferryland) on the west by a narrow isthmus. The Downs can be considered as a sloping land covered in grass and its marine landscapes range from cobble and sandy beaches to sheer rock cliffs (Watton 2016). The land to the east of The Downs narrows to form another isthmus connecting its main part to Ferryland Head where the peninsula turns south, and low shrubs, mosses, and wetlands dominate. The Ferryland Head formation is the eastern extreme of the peninsula with the historic Ferryland Head Lighthouse on the Atlantic coast cape.

The Ferryland supersite consisted of three separate measurement sites. The Downs and Battery sites (Fig. 1) were the two most densely instrumented observational sites in the Ferryland cluster (see also Gultepe et al. 2021 and Perelet et al. 2021). The centrepiece of the University of Notre

Dame (UND) turbulence program was a 16.2-m flux tower erected at The Downs (47°01'17.1"N and 52°52'19.5"W) to examine air–sea/land coupling in the coastal zone with and without fog (Fig. 1). We use 15-min-averaged turbulent, surface meteorology, and visibility data collected at the UND flux tower from 1 September through 6 October 2018. Surface meteorology, turbulent fluxes of momentum, sensible and latent heat and other relevant turbulent statistics were measured continuously at four levels (Fig. 2), nominally 2, 5, 10, and 15 m above ground level (a.g.l.). The UND flux tower base ("ground level" for this tower) is elevated to about 32 m above sea level. Each measurement level was instrumented with identical fast-response three-axis sonic anemometers sampling wind velocity and sonic temperature at 20 Hz (Young Model 81000, R.M. Young Company, Traverse City, MI, USA) and temperature and relative humidity (T/RH) probes at sampling frequency = 1 Hz (Rotronics HC2S3, Campbell Scientific, Inc., Logan, UT, USA). The HC2S3 probes were housed in ventilated radiation shields. A fast-response (20 Hz) open path infrared gas analyzer (LI-7500A, LI-COR Biosciences, Lincoln, NE, USA) was collocated with a sonic anemometer at 5-m height for direct measurement of water vapour and carbon dioxide turbulent fluxes and other relevant H_2O and CO_2 turbulence statistics. In addition, an optical sensor (Present Weather Detector and Visibility Sensor, PWD22, Vaisala Corp., Helsinki, Finland) mounted on a boom at an intermediate level between 2-m and 5-m instrument levels was used for direct measurements of visibility, precipitation intensity, and precipitation type. Measurements were stored on a data logger (Campbell CR3000, Campbell Scientific, Inc., Logan, UT, USA) and successively parsed into 15-min data files.

The flux tower was also instrumented with radiometers for measurements of the downwelling and upwelling shortwave and longwave radiation (CMP, Kipp & Zonen, Delft, the Netherlands). Soil temperature and soil heat flux were measured by soil temperature probes and heat flux plates buried in the vicinity of the flux tower. Other ancillary instruments at The Downs site included but are not limited to sodars/RASS, lidars, and scintillometers. However, the current study focuses on theanalysis of atmospheric small-scale turbulence and these measurements are not included in the discussion.

The mean wind speed and wind direction were derived from the sonic anemometers, with rotation of the anemometer axes needed to place the measured wind components in a streamline coordinate system based on 15-min-averaged 20-Hz data. We used the most common method, which is a double rotation of the anemometer coordinate system, to compute the longitudinal, lateral, and vertical velocity components in real time. (Kaimal and Finnigan 1994, Sect. 6.6). All directions for wind and surface stress in the paper are calculated using the meteorological convention ("from"), i.e. the direction from which the wind is blowing. The measurements of air temperature and relative humidity at several levels provided by T/RH probes were used to evaluate the vertical temperature and humidity gradients based on 15-min-averaged 1-Hz data. Turbulence covariance and variance were derived from the sonic anemometer/thermometers through frequency integration of the appropriate cospectra and spectra computed from 13.65-min data blocks (corresponding to 2^{14} data points) from the original 15-min data files. The dissipation rate of turbulence kinetic energy (TKE) as well as the destruction rate of half the temperature (humidity) variance were estimated as in Grachev et al. (2015, 2016).

A correction term (called the Webb effect following Webb et al. 1980) was applied to the computed water vapour and carbon dioxide turbulent fluxes. In particular, the turbulent flux of carbon dioxide was computed based on the instantaneous mixing ratio of the trace gas relative to dry air according to the density correction theory of Webb et al. (1980, their Eq. 20). In the case of a "fast" mixing ratio-based flux (i.e., converting the raw data point-by-point to mixing ratios), the true turbulent flux of carbon dioxide could be expressed in pure eddy-covariance form (see Grachev et al. 2011 for discussion).

Several data-quality indicators based on objective and subjective methods have been applied to the original flux data in order to remove spurious or low-quality records. In particular, turbulence data have been edited for unfavourable relative wind directions, non-stationarity, mean wind vector tilt, minimum or/and maximum thresholds for turbulent statistics etc. Based on established criteria, the best flux estimates have been used. The filtering criteria adopted in this study are described in Grachev et al. (2015, 2016, 2018b, and references therein). In addition, an observational record is considered as a low-quality record when the skewness is outside the range [–2, 2] or the kurtosis is outside the range [1, 8] (Vickers and Mahrt 1997). Recall that the skewness and the kurtosis of a standard normal (Gaussian) distribution are zero and three respectively. Skewness and kurtosis values of wind components, sonic temperature, and specific humidity (measured by the LI-7500A gas analyzer) outside this range represent the data records that are beyond normal physical expectations. Skewness and kurtosis spikes may be associated with a situation when optical windows (LI-7500A) and sonic transducers were contaminated by water due to precipitation, fog, or dew. Other details of the turbulent measurements, turbulent data processing, accuracy, calibration, and data-quality criteria can be found in Grachev et al. (2011, 2015, 2016, and 2018a, b).

The total data after averaging for a sonic anemometer at level 4 (15 m a.g.l.) amounts to 3456. After data-quality control screening, that number decreases to 2481 (≈ 72% of the original amount). These 2481 data include 2189 no-fog data and 292 fog data (≈ 12%). Additional restriction on the spectral slopes in the inertial subrange described in the Sect. 4.2 (only for the computation of the dissipation rate of TKE, ε) decreased the amount of data further from 2481 to 1296 (≈ 37% of the original amount 3456).

Although it is important to estimate the influence of foggy and cloudy conditions on the measurements by a sonic anemometer, this topic is often not discussed in the literature and there are only few works on this subject. According to Siebert and Teichmann (2000), measurements under foggy (or cloudy) conditions gave no significant hint on such an influence. In particular, the observed deposition of water droplets on sonic anemometer transducers had no significant influence on wind speed. Even the power spectra of horizontal velocity components show a very similar behaviour under dry and foggy (or cloudy) conditions, displaying the classical –5/3 Kolmogorov power law at high frequencies. El-Madany et al. (2013) found that, in general, differences in resulting fluxes between foggy and non-foggy conditions are usually smaller than the flux error of the measurements. According to El-Madany et al. (2013) measurements, all sonic anemometers tested in the study produce more spikes under foggy conditions compared with conditions without fog, and sonic spectra and cospectra show white noise in the high-frequency range during dense fog. However, this is no cause of concern regarding data quality in general.

3 Turbulence Measurements at The Downs site in Ferryland

In this section, we provide a general description of turbulence and mean meteorological data collected at four levels of the UND flux tower located at The Downs measurement site (see also Sect. 2). In particular, we analyze the time series and dependence on wind direction of various parameters. This allows study of temporal and spatial structure of the ABL in the coastal zone in detail, providing general insights into the nature of air–sea/land coupling in an area of complex terrain before focusing on fog cases.

3.1 Time Series

Here, we analyze the time series of 15-min-averaged surface fluxes and basic meteorological variables to describe weather conditions, turbulent exchange, and other relevant variables for the period from 1 September through 6 October 2018. This corresponds to the year days from 244 through 279 with respect to 1 January 2018 UTC. Local time in Ferryland during the C-FOG field campaign was Newfoundland Daylight Time (NDT) that was 2.5 hours behind UTC. Figures 3 and 4a show the time series of 15-min-averaged basic meteorological variables collected at The Downs site in Ferryland (the UND flux tower). As mentioned in Sect. 2, the wind speed (Fig. 3a) and wind direction (Fig. 3b) are based on the sonic anemometer measurements (20-Hz sampling rate), whereas the air temperature (Fig. 3c), relative humidity (Fig. 3d), and visibility (Fig. 4a) data are based on the slow-response sensors.

Figure 4a shows 15-min-averaged visibility measured by the PWD22 sensor at The Downs observational site. A clear sky with high visibility (i.e., fog-free events) corresponds to the maximum visibility measurable with the instrument (PWD22) which is 20 km (Fig. 4a). Fog events reduce the visibility to 1 km (fog definition) and less (e.g., Vautard et al. 2009), and during the heavy fog time periods, the visibility was about 100 m (Fig. 4a). The observed relative humidity values were close to 100% during fog conditions (Fig. 3d).

The turbulent fluxes of momentum (or magnitude of the wind stress), τ, sensible heat, H_S, and latent heat, H_L, can be estimated by using the eddy-correlation method according to

$$\tau = \tau_x \equiv \rho u_*^2 = -\rho \overline{w'u'} \ , \tag{1}$$

$$H_S = c_p \rho \overline{w'\theta'} \ , \tag{2}$$

$$H_L = \mathcal{L}_e \rho \overline{w'q'} \, , \tag{3}$$

where u_* is the friction velocity, ρ is the mean air density, θ is the air potential temperature, q is the air specific humidity, c_p is the specific heat capacity of air at constant pressure, and $\mathcal{L}_e$ is the latent heat of evaporation of water. Here, w is the vertical velocity component, the prime [$'$] denotes fluctuations about the mean value, and an overbar is an averaging operator (15 min in this study). In Eq. 1, $\tau_x = -\rho \overline{w'u'}$ represents the longitudinal (or downstream) component of wind stress. Note that the traditional MOST assumes that stress and wind vectors are aligned in the same direction, i.e. the lateral (or crosswind) stress component $\tau_x = -\rho \overline{w'v'} = 0$ by definition (v is the lateral velocity component). Thus, u_* should be computed based on the downstream component of the wind stress (τ_x) only for purposes of verification and validation of MOST (see Grachev et al. 2011 for further discussion).

Time series of u_*, H_S, and H_L defined by Eqs. 1–3 for the 15-min-averaged turbulence data observed at four levels of the UND flux tower at The Downs site are shown in Fig. 4b, c, d respectively. The traditional sign convention for the sensible heat (Fig. 4c) is used: $H_S < 0$ corresponds to stable conditions, or a stable boundary layer (SBL) and $H_S > 0$ to unstable conditions or a convective boundary layer (CBL). According to Fig. 4c, the near-surface atmosphere is mostly unstable during local daytime ($H_S > 0$), whereas at night the near-surface environment is generally stably stratified ($H_S < 0$). It is obvious that friction velocity (Fig. 4b) and the wind speed (Fig. 3a) are highly correlated to one another. During a fog event the moisture flux data can become irregular and the latent heat flux is often negative (corresponding to a downward moisture flux). Such behaviour of H_L reflects the complexity of the physical processes that control the genesis, evolution, advection, and dissipation of fog. In particular, the turbulent transfer of moisture downward to the surface (negative latent heat flux) is associated with removing moisture from the foggy air layer, e.g., due to condensation of the water vapour on the land surface. The result ($H_L < 0$) is generally consistent with the previous observations over coastal waters by Edson et al. (2007, Fig. 18), Heo et al. (2010, Figs. 4, 5, 9), and Huang et al. (2015, Fig. 6).

Although the temporal course of surface meteorology and the surface fluxes in Figs. 3 and 4 at different instrument levels are qualitatively very similar, there are noticeable differences associated with the different aerodynamic and thermal properties of the underlying surface footprint. According to Fig. 4b, amplitude of the 15-min-averaged friction velocity at the lower level 1 is generally higher than that at the upper levels (especially at levels 3 and 4 located at 10 and 15 m a.g.l., respectively). This may be attributed to the fact that the upper sonic anemometers correspond to relatively smoother sea-surface footprints (or mixed sea and land footprints) whereas u_* observed at the lower level 1 is associated with a rough inland footprint.

Additionally, values of both the sensible and latent heat fluxes display marked differences when measured over water footprints as compared to over land footprints. First, magnitudes of H_S, and H_L observed over sea-surface footprints are somewhat lower than H_S and H_L measured over land footprints (see Fig. 4 for different time intervals). Furthermore, there is a pronounced diurnal cycle evident in H_S and H_L observed, for example, during the year days 250–255 (corresponding to rough inland footprints), whereas for H_S and H_L associated with a relatively smooth sea-surface footprints (e.g., during the year days 256–258) such a cycle is only marginally observed (Fig. 4). Such differences in diurnal cycles of H_S and H_L as measured over different surfaces can be attributed to different specific heat capacities between water and land associated with different wind directions, discussed in the next section.

A sharp change from rough to smooth surfaces (and vice versa) can lead in general to complex vertical structure of aerodynamic flow where turbulent fluxes vary rapidly with height even in the lowest few metres. According to Mahrt et al. (2018), the flow response to such changes of surface roughness is generally associated with a formation of the three-layer structure, which includes a shallow "new" boundary layer at the surface, an overlying "regional boundary layer", and the transition layer between these two layers (Mahrt et al. 2018, Fig. 5). In such conditions, the vertical divergence (or convergence) of the momentum and heat fluxes often can be large near the surface where it is assumed that the turbulent fluxes are constant with height and equal to the surface values (concept of the surface or constant-flux layer). Thus, measurements at standard observational levels (2–10 m) are inadequate for estimation of the surface fluxes in such situations (Mahrt et al. 2018).

3.2 Dependence on Wind Direction

The interpretation of atmospheric turbulence measurements depends largely on an upwind 'flux footprint' (or 'source area') over which the turbulent fluxes and other statistics are sampled. Generally the flux footprint is a surface area at some distance from the tower upwind (fetch), which contains effective surface characteristics contributing to a measured signal (Kljun et al. 2004, 2015; Burba 2013; Leclerc and Foken 2014). In other words, the flux footprint is an area "seen" by a sensor at a tower (field-of-view). Traditionally, the relationship between the surface flux in an upwind source area (at z = 0) and the flux measurement point at reference height z (where sensors are located) are formalized via the footprint function, which depends on measurement height, upwind and crosswind distance, thermal stratification, and surface roughness.

The complexity of the coastal environment in Ferryland (Fig. 1) makes analysis of turbulence data difficult. This is due to the fact that because of the surface heterogeneity, turbulence parameters become functions of the wind direction and, therefore, surface footprints. As a result, instruments mounted at different levels even at the same tower can have very different footprints: a relatively smooth sea surface or aerodynamically rough dry inland areas. In this subsection, the visibility, the drag coefficient, the sensible and latent heat fluxes are analyzed as a function of wind direction (Fig. 5). The dependence on wind direction of various parameters can also shed light on the time series behaviour of the surface fluxes and surface meteorology shown in Figs. 3 and 4 for the entire field campaign.

According to our data, weather conditions favourable for fog at The Downs site (low visibility in Fig. 5a) occur predominantly with onshore surface flow from north-east to north-north-east ($\approx 30°$) and from south-east to south-south-east ($\approx 210°$). Recall that The Downs is a land strip stretched from about north to south (Fig. 1), thus the fog in these cases formed over ocean water and moved into land areas (marine advection fog).

Traditionally, the turbulent fluxes (1)–(3) are parametrized by bulk aerodynamic relationships, which relate fluxes to mean properties of the flow through the height-dependent transfer coefficients. In particular, the turbulent flux of momentum, $\tau = \rho u_*^2$, is typically formulated using the drag coefficient defined as

$$C_D = \frac{\tau}{\rho U^2} = \left(\frac{u_*}{U}\right)^2 \quad , \tag{4}$$

where τ is based on the uw-covariance, Eq. 1, and U is the mean wind speed at reference height z, derived from a sonic anemometer in the current study. Note that the drag coefficient (4) is traditionally adjusted to the 10-m neutral drag coefficient using MOST and C_D is closely related to aerodynamic roughness length, z_0, through its neutral counterpart C_{Dn} (see, for example, Grachev et al. 2011). Although z_0 is not a physical length, it is typically related to the height of terrain roughness elements (physical roughness of the underlying surfaces). As mentioned above, the drag coefficient and roughness length over a rough land surface differ widely from over-sea-surface values. Observations of wind stress and wind speed over the ocean reported in the literature indicate that $C_D \approx 1.0{\cdot}10^{-3} - 1.3{\cdot}10^{-3}$ (e.g., Fairall et al. 2003). Meanwhile, the average C_D values over land areas can be an order of magnitude larger than over the sea due to a relatively large aerodynamic roughness of the land surface (e.g., Grachev et al. 2011; 2018a).

Figure 5b shows the drag coefficient C_D as a function of true wind direction measured at the four tower levels. According to Fig. 5b, the drag coefficient (4) is very sensitive to the wind direction, because a change in wind direction results in sampling of very different upwind surface characteristics. In addition, the drag coefficient in Fig. 5b depends on the height of the measurement. Values of C_D measured by two upper sonic anemometers (levels 3 and 4) correspond in general to sea-surface footprints ($C_D \sim 10^{-3}$) whereas C_D observed at the lower level 1 is associated with the rough inland footprints (level 2 shows mixed behaviour). We note however that C_D might decrease with height due to the vertical divergence of the momentum flux (e.g., Mahrt et al. 2018) and further investigation is needed to verify changes of C_D with height for this case. The exception is for flow from the sector between $\approx 80°$ and $\approx 130°$ (easterly winds) and in the sector between $\approx 280°$ and $\approx 330°$ (westerly winds); that is, along The Downs land formation (Fig. 1). These sectors are shown in Fig. 5 as vertical dotted lines. In these cases, the values of C_D observed at all four levels correspond to rough inland footprints (Fig. 5b). Another noteworthy case is associated with the behaviour of the drag coefficient (elevated C_D) observed at level 1 for onshore winds originating between $\approx 220°$ and $\approx 280°$ (Fig. 5b). One can assume this sharp change in C_D is due to the influence of individual obstacles such as a sharp-edged coastal cliff from south-west and west-south-west. Moreover, the drag coefficient also increases dramatically where a nearby obstruction (e.g., another instrument, lab trailer) is immediately upwind of a sonic anemometer or when an instrument is within a deep roughness sublayer.

The plots of the sensible heat, H_S, and latent heat, H_L, fluxes versus wind direction also show a strong wind direction dependence in general (Fig. 5c, d respectively). According to Fig. 5c, d, magnitudes of both the sensible and latent heat fluxes are generally less for the wind-direction sectors associated with the over-water footprints as compared to over-land footprints. The different behaviour of the turbulent energy fluxes in Fig. 5c, 5d for different wind directions is perhaps due to the different heat capacity and thermal conductivity between water and land, allowing stronger diurnal variations of H_S and H_L fluxes that develop over land (see also time series of H_S and H_L in Fig. 4c, d). Note that a negative (downward) latent heat flux, $H_L < 0$, associated with onshore winds in the direction sectors from the north-east to the north-north-east and from the south-west to the south-south-west (Fig. 5d) was mainly observed during the fog events (cf. Fig. 5a).

4 Turbulence Measurements in the Coastal Zone in the Presence/Absence of Fog

In this section we focus on the boundary-layer turbulence during fog events and compare them with similar characteristics observed for non-fog conditions. First, we consider the longest fog event of the C-FOG field campaign at The Downs site in detail (Sect. 4.1). In Sect. 4.2, we estimate the impacts of fog on turbulence scaling laws.

4.1 Case Study of Fog Event during 27–30 September 2018

While most of the instruments at Ferryland and other C-FOG observational sites acquired data continuously (e.g., see Figs. 3 and 4), the data streams have been enhanced periodically by additional measurements (e.g., tethered balloons, extra radiosonde launches per day) during short periods of research activities referred to as intensive operational periods (IOPs). The entire C-FOG field campaign included 12 IOPs (with and without fog events) where all instruments were operated in coordination (see Fernando et al. 2021, Table 1a). A typical IOP was a day long or less, except one long IOP-10 (27–30 September 2018) that lasted about 3 days with extended foggy periods.

The long IOP-10 started at 1730 UTC (1500 NDT) 27 September and ended at 0330 UTC 30 September (2018 year days 270–273), and was an illustrative example of how turbulence in the coastal zone differs between fog and non-fog conditions. Data collected during IOP-10 provided comprehensive multiday information on microphysical, optical, turbulent, and environmental variables at multiple levels. Photos in Fig. 6 give visual evidence for fog at The Downs site during IOP-10. The pictures were taken just before local noon (1430 UTC) 29 September 2018 and show the UND flux tower and the instruments shrouded by heavy fog. To show contrast with a clear day (Fig. 2), some pictures in the presence of fog (Fig. 6) were taken at approximately the same spot and viewing angle to compare visibility in the presence and in the absence of fog (cf. Fig. 2a versus Fig. 6a and Fig. 2c versus Fig. 6c).

Figures 7 and 8 show the time series of 15-min-averaged surface meteorology, surface fluxes, visibility, and turbulence properties data taken at the UND flux tower at The Downs from 27 September to 3 October (2018 year days 270–276). This time period includes a fog event observed during the Super IOP-10 (year days 270–273) and an additional couple days without fog (year days 274–276). The unusually long fog event on 28–30 September was due to the interaction of two large synoptic scale features: a deep polar low to the north (in northern Canada) and a tropical cyclone to the south (in the Central Mid-Atlantic) connected by a saddle point to the south of Ferryland (Dorman et al. 2021). Visibility measurements at The Downs site in Ferryland by the PWD22 sensor (Fig. 7b) indicated two regions of low visibility during 28 September (year day 271) and lengthy foggy conditions during almost the entire day of 29 September (year day 272) that dissolved after around 1200 UTC on 30 September (year day 273). During the IOP-10, the PWD22 device also reported rain events accompanied by precipitation fog that forms when rain is falling through cold air (see Fernando et al. 2021 for further details). The foggy periods in Fig. 7b are normally associated with a saturated atmosphere and a relative humidity near 100% (see Fig. 7g).

Apart from the obvious difference in visibility and relative humidity, there are noticeable differences in the sensible and latent heat fluxes observed during fog events as compared to non-fog conditions. First, there is a well pronounced diurnal cycle in sensible heat during clear days year days 274 and 275 (Fig. 7f) compared to foggy conditions (year days 271–273). Furthermore, there is a marked difference in the behaviour of the latent heat flux in the presence and absence of fog. According to Fig. 7h, during the year days 271–273 fog event the latent heat flux data become irregular and H_L is often negative (cf. Edson et al. 2007, Fig. 18). Other examples of similar behaviour of H_S and H_L in the presence and absence of fog can be found in the time series of H_S and H_L for the entire campaign (Figs. 4c and 4d), e.g. during IOP-7, 16–17 September (year days 259–260).

Time series of the standard deviations (σ_w, σ_θ, σ_q), drag coefficient (C_D), TKE, and dissipation rate of TKE (ε) are shown in Fig. 8. Signatures of fog are evident as perturbations to the standard deviation of water vapour concentration (and to some extent standard deviation of air temperature) when the time series of σ_q and partially σ_θ data become irregular during the year days 271–273 fog event (Fig. 8e, c respectively). However, fog has no obvious influence on the other variables such as σ_w, C_D, TKE, and ε (Fig. 8). In addition, variations of the dimensional turbulence statistics shown in Fig. 8 may be associated with the variations of the wind speed (Fig. 7a) and wind direction (Fig. 7b) during this period and on this background it is difficult to see the real correlation with fog. To separate influences of fog and wind speed on dimensional turbulence statistics, we evaluated the properly scaled non-dimensional standard deviations and the dissipation rate derived from the data collected separately for fog and non-fog conditions. Furthermore, the time series of surface meteorology and statistics of turbulence with higher temporal resolution collected at The Downs site in Ferryland during IOP-7 can be found in Fernando et al. (2021, Fig. 7) and Bardoel et al. (2021, Fig. 6).

The coastal zone is generally complicated by momentum or/and thermal internal boundary layers (IBL) that form due to discontinuities of aerodynamic and thermal surface properties at the coastline that modify onshore or offshore advection of air. The surface heterogeneity produces a complex vertical structure where turbulence parameters such as C_D and H_S become functions of a measurement height and/or direction and, therefore, the surface footprint. Under such conditions, the flow at greater heights becomes partially decoupled from the surface. Figures 7 and 8 show a noteworthy case of a thin convective IBL resolved by the tower during the year days 270.4–270.8 (no fog) for flow from the south-west ($\approx 225°$) (Fig. 7c). Our measurements show that the sensible heat fluxes measured by the two upper sonic anemometers (levels 3 and 4) correspond to stable stratification, $H_S < 0$, whereas H_S at two lower levels 1 and 2 corresponds to unstable conditions, $H_S > 0$ (Fig. 7f). The occurrence of such a thin convective IBL in a statically stable ABL was observed with onshore winds (sea breeze) that blow over a relatively cold sea onto heated land during the day. Another case of a thin convective IBL but under foggy conditions was observed during the year day 272.4–272.8 (Fig. 7f) for approximately the same onshore south-westerly wind directions (Fig. 7c).

We also observed the opposite situation where advection of onshore air from warm water toward the cooler land (usually at night) leads to formation of a shallow stable IBL with a region of unstable stratification above. Measurements for onshore winds in the sector from $\approx 0°$ to $\approx 90°$ (mainly with north-easterly prevailing winds) during the year days D 261.5–265 (Fig. 3b) show several episodes of the shallow stable IBLs. Values of $H_S > 0$ (Fig. 4c) and $C_D \sim 10^{-3}$ (not shown) measured by two upper sonic anemometers (levels 3 and 4) correspond to convective conditions and sea surface footprint whereas $H_S < 0$ (at night) and $C_D \sim 10^{-2}$ observed at the lower level 1 correspond to the stable stratification and rough inland footprints. At the same time, the level 2 shows $H_S \approx 0$ (near-neutral stratification) and mixed behaviour of the drag coefficient for these cases. This sharp vertical change in H_S and C_D due to the different surface types shows that in these cases the IBL height is between sonic anemometers at levels 2 and 3 (between 5 and 10 m a.g.l. respectively) or close to level 2.

4.2 Verification of Monin–Obukhov Similarity in the Coastal Zone with and without Fog

In almost all numerical weather prediction and climate models, surface turbulence fluxes and other parameters are parametrized using MOST and/or a bulk flux algorithm. Below, we evaluate MOST predictions using data collected during the entire C-FOG field campaign at The Downs observation site separately for fog events and non-fog conditions (i.e., during clear sky days with high visibility).

According to MOST, any properly scaled statistics of turbulence at reference height z are universal functions of a stability parameter $\zeta = z/L$ defined as the ratio of z and the Obukhov length scale, L (Obukhov 1946):

$$\zeta = -\frac{\kappa g z}{\theta_v}\frac{\overline{w'\theta_v'}}{u_*^3}, \tag{5}$$

where θ_v is the virtual potential temperature, g the acceleration due to gravity, and κ the von Kármán constant. Specifically, the non-dimensional standard deviations of wind speed components can be written as

$$\varphi_\alpha(\zeta) = \frac{\sigma_\alpha}{u_*}, \tag{6}$$

where α ($= u$, v, and w) denotes the longitudinal, lateral, and vertical velocity components respectively. Similarly, standard deviations for scalars, the air temperature, σ_θ, and the specific humidity, σ_q, are scaled as

$$\varphi_\theta(\zeta) = \frac{\sigma_\theta}{|\theta_*|}, \tag{7}$$

and

$$\varphi_q(\zeta) = \frac{\sigma_q}{|Q_*|}, \tag{8}$$

where $\theta_* = -\overline{w'\theta'}/u_*$ and $Q_* = -\overline{w'q'}/u_*$ are the temperature and the specific humidity scales respectively. The dissipation rate of TKE, ε, in the MOST framework is expressed as

$$\varphi_\varepsilon(\zeta) = \frac{\kappa z \varepsilon}{u_*^3}. \tag{9}$$

Figures 9 and 10 show the normalized standard deviation for all three velocity components (6) plotted versus the local stability parameter, $\zeta = z/L$ evaluated at each observational level (local scaling) for both stable and unstable conditions. The left panels (Fig. 9a, c, e, g and Fig. 10a, c, e, g) present unstable ($\zeta < 0$) conditions, and the right panels (Fig. 9b, d, f, h and Fig. 10b, d, f, h) stable ($\zeta > 0$) conditions. Figure 9 shows non-fog conditions whereas Fig. 10 shows foggy conditions. We have imposed the visibility threshold to 6 km to separate the turbulence data into two categories (fog and no fog). In this study, by foggy conditions we mean fog itself (visibility less than 1 km) and mist (visibility between 1 and 6 km). This classification was suggested by Dorman et al. (2021) based on the data collected during the C-FOG field campaign including the Ferryland/Downs and Ferryland/Battery measurement sites. Similar plots of the normalized dissipation rate of TKE (9), air temperature (7), and specific humidity (8) plotted versus $\zeta = z/L$ are in Fig. 11 and Fig. 12 for fog-free and foggy conditions, respectively. The dissipation rate of TKE ε in (9) was estimated using the common inertial-dissipation method that assumes the existence of an inertial subrange associated with a Richardson–Kolmogorov cascade. As mentioned in Sect. 2, the data where the spectral slope in the inertial subrange deviated more than 20% of the theoretical -5/3 slope were excluded from the analysis for both fog-free and foggy conditions (only for estimation of ε). Note that Ortiz-Suslow et al. (2019, 2020) suggested that there may be natural deviations from Kolmogorov's turbulence over the ocean that occur within ±20% of the -5/3 slope and this could have implications for the spectrally derived dissipation rate estimates. According to Ortiz-Suslow et al. (2020), these variations in the inertial subrange bandwidth and spectral slope may be driven, in part, by mechanical wind–wave interactions.

According to Fig. 9, the non-dimensional universal functions (6) for all three velocity components measured in the coastal zone during the non-fog conditions, on the average, follow MOST local scaling for both stable ($\zeta > 0$) and unstable ($\zeta < 0$) stratifications. Commonly, our results in Fig. 9 are in good agreement with our previously reported values of $\varphi_w(\zeta)$ and $\varphi_u(\zeta)$ measured in North Carolina's coastal zone near the seaside town of Duck during the CASPER-East field campaign during October–November 2015 (Grachev et al. 2018a, Figs. 7 and 8). However, our observations at The Downs site show larger scatter of individual data-points for the universal functions (6) as compared with the CASPER-East measurements. This is likely associated with the complexity of the coastal landforms of Ferryland compared to the Outer Banks near Duck, North Carolina. As expected, the neutral-stability asymptotic limits shown in Fig. 9 follow $\varphi_w(0) < \varphi_v(0) < \varphi_u(0)$ associated with the anisotropy of airflow in the near-neutral regime. The present results for near-neutral stabilities $\varphi_u(0) = 2.3$, $\varphi_v(0) = 1.8$, and $\varphi_w(0) = 1.25$ (Fig. 9) are consistent with our previous findings of the CASPER-East field campaign (Grachev et al. 2018a).

The non-dimensional standard deviations of the velocity components (6) measured during the low-visibility conditions when the PWD22 visibility was less than 6 km (fog and mist) also follow MOST predictions with surprisingly small scatter (Fig. 10). Furthermore, the data for different measurement levels collapse fairly well into a single universal curve, especially for $\varphi_w(\zeta)$ (Fig. 10a, b). Scatterplots of individual 15-min-averaged values of the scaled universal functions (7)–(9) in Fig. 11–12 show generally larger scatter than for plots of the non-dimensional functions (6) in Figs. 9–10. Although the scatter is large enough for $\varphi_\varepsilon(\zeta)$, $\varphi_\theta(\zeta)$, and $\varphi_q(\zeta)$ universal function (Fig. 11–12), there is no substantial difference between fog (Fig. 12) and no-fog (Fig. 11) cases on the average, perhaps with the exception of $\varphi_q(\zeta)$. Observations show poor correspondence of $\varphi_q(\zeta)$ with MOST in fog; the statistical dependence of $\varphi_q(\zeta)$ on the MOST stability parameter (5) is weak, if not non-existent (Fig. 12e, f). Additionally the data scatter for $\varphi_q(\zeta)$ is somewhat greater for foggy events (Fig. 12e, 12f) as compared with the no-fog conditions events (Fig. 11e, f).

Note that the behaviour of $\varphi_\theta(\zeta)$ for near-neutral conditions $|\zeta| \to 0$ is ambiguous (Fig. 11c, d) because the temperature scale θ_* is small and asymptotically tends to zero as ζ approaches zero, whereas, in the near-neutral case the value of σ_θ is small but still finite (see discussion in Grachev et al. 2018a). This point is less true for σ_q and $\varphi_q(\zeta)$, where $|Q_*|$ need not be small in neutral conditions. This behaviour of σ_θ and σ_q is associated with a surface that is thermally inhomogeneous and non-uniform in water content wherein local hot and cold and/or wet and dry spots on the surface generate small-scale advection which enhances σ_θ and σ_q but generally not the surface fluxes, i.e., θ_* and Q_*. Thus, the Ferryland/Downs C-FOG data for $\varphi_\theta(\zeta)$ and $\varphi_q(\zeta)$ systematically overestimate the empirical Kansas-type expressions by Kaimal and Finnigan (1994, Eq. 1.34) due to spatial heterogeneity of aerodynamic and thermal/water properties of the underlying coastal surfaces. Note, that this behaviour of $\varphi_\theta(\zeta)$ and $\varphi_q(\zeta)$ (for both fog and non-fog cases) is consistent with our previous measurements in the coastal zone (Grachev et al. 2018a, Fig. 9).

Although the physical mechanisms involved with fog formation, evolution, and dissipation may affect turbulent transport and turbulence parameters such as the standard deviations and the TKE dissipation rate, the non-dimensional forms of these parameters (6)–(9) are less affected by fog, especially $\varphi_w(\zeta)$ (cf. Fig. 9a, b with Fig. 10a, b respectively). This may be due to the fact that fog-related changes of σ_w (or TKE) and ε, for example, are accompanied by changes of u_* at the same time (see Figs. 7d, 8d, f) resulting in the universal functions (6) to closely follow the canonical MOST predictions for fog and no-fog cases (Figs. 9 and 10). The situation with the scalars (air temperature and especially specific humidity) is not so straightforward. In particular, the life cycle of fog water is associated with evaporation and condensation of water droplets, i.e., the phase transition of liquid water to water vapour and vice versa. Evaporation absorbs latent heat and cools the surrounding air while condensation releases latent heat and warms the surrounding air, thus introducing additional temperature and humidity fluctuations that lead to deviation from MOST for $\varphi_\theta(\zeta)$ and $\varphi_q(\zeta)$ because the phase transition violates assumptions underlying the MOST.

A detailed discussion of the non-dimensional profiles of wind speed, $\varphi_m(\zeta)$, and temperature, $\varphi_h(\zeta)$, (the flux-profile relationships) lies beyond the scope of this study. Our previous observations (Grachev et al. 2018a) showed poor (if not non-existent) statistical dependence of $\varphi_m(\zeta)$ and $\varphi_h(\zeta)$ on the MOST stability parameter $\zeta = z/L$ in the coastal zone due to non-local mixing. According to Grachev et al. (2018a), suitably scaled non-dimensional profiles of wind speed and temperature vary significantly among different observation levels and often the vertical fluxes can be counter to local gradients.

Although the data presented in Figs. 9–12 generally proves the validity of the Monin–Obukhov approach, these plots can be affected by self-correlation because the same variables (primarily the friction velocity, u_*) appear both in the definitions of the universal functions (6)–(9) and in $\zeta = z/L$. However, the self-correlation can be overcome, for example, by plotting a universal function or stability parameter in a "hybrid" representation without u_* (e.g., Grachev et al. 2018a, Fig. 13 and references therein). This method is based on the idea that a combination of any Monin–Obukhov universal functions is itself a universal function. For example, universal functions φ_m/φ_w, φ_w/φ_u, $\varphi_\varepsilon/\varphi_w^3$ among others plotted versus $\zeta = z/L$ by definition are not affected by the self-correlation because a new universal function shares no variables with the MOST stability parameter (5). According to Grachev et al. (2018a, Fig. 13), the scatter of the data around the empirical Kansas-type expressions does not change substantially so that the self-correlation likely would not affect the general results obtained in a coastal zone. Similar approach can be also applied to current study to mitigate the self-correlation issue (not shown).

5 Summary and Discussion

This observational study dealt with an analysis of small-scale atmospheric turbulence based on measurements in the coastal zone near the town of Ferryland, Newfoundland, during the C-FOG Program (September–October 2018). The campaign periods were selected based on the climatology of the area (Dorman et al. 2017, 2020). The measurement site, named The Downs, is located on a long peninsula just east of Ferryland (Fig. 1). Turbulence and mean meteorological data were collected at multiple levels on the 16.2-m flux tower deployed on land in close proximity of the shoreline to examine air–sea/land coupling with and without fog (see Figs. 2 and 6). Detecting fog and precipitation at The Downs site was based on the visibility measurements by a Vaisala PWD22 optical sensor mounted on the flux tower. Instruments, data collection, and site description are documented in Sect. 2. In Sect. 3, the time series of various parameters and their dependence on wind direction during the entire field campaign (from 1 September through 6 October 2018) were presented. The analysis of basic meteorological parameters, turbulent fluxes, TKE and its dissipation rate, and scaling laws for the coastal zone with and without fog are described in Sect. 4.

Both stable and unstable shallow internal boundary layers (IBLs) were resolved by the flux tower measurements with the IBL height located between sonic anemometers at levels 2 and 3 (between 5 and 10 m a.g.l., respectively) or even close to the level 2. The advection of onshore winds (sea breeze) from a relatively cold sea toward the heated land (usually during the day) provided conditions for convective IBL in a statically stable ABL. A shallow stable IBL with unstable stratification aloft was observed during onshore winds blowing from over warm waters toward cooler land that typically occurred during the night. Note that in numerical weather prediction and climate models, the lowest computational level extends above the IBL, and thus IBL gradients that are prominent in air–sea/land exchange cannot be resolved by the models due to insufficient grid resolution.

Our study was primarily focused on the applicability of Monin–Obukhov similarity theory (MOST) for the coastal zone for fog and no-fog conditions. Despite the existence of a substantial body of literature on fog research (Lewis et al. 2004; Gultepe et al. 2007, 2009; Koračin et al. 2014; Koračin and Dorman 2017 and references therein), turbulent fluxes and other statistics as well as scaling laws for foggy costal ABLs have not been systematically examined.

The 15-min-averaged turbulent fluxes and basic meteorological variables were analyzed first for year days from 270 to 276 (from 27 September to 3 October 2018), which included the longest IOP of the campaign (IOP-10; days 270–273) with fog lasting about two days and additional days without fog (year days 274–276). There were noticeable differences in the behaviours of sensible and latent heat fluxes between fog and no-fog conditions. There was a well pronounced diurnal cycle in sensible heat over land during clear days, whereas with fog the diurnal cycle was much weaker in amplitude (Fig. 7f). Under foggy conditions the moisture-flux data behaved erratically (Fig. 7h) and the latent heat flux was often negative corresponding to a downward moisture flux. The $H_L < 0$ result is generally consistent with previous observations over coastal waters by Edson et al. (2007), Heo et al. (2010), and Huang et al. (2015). However, the negative latent heat flux, in general, is somewhat rare and occurs only during certain configurations of air and surface conditions.

The impacts of fog on the scaling laws for single-point turbulence statistics such as the scaled non-dimensional standard deviations of velocity components, scalars, and the dissipation rate of TKE were also studied (Sect. 4.2). In this study (Figs. 10 and 12), we describe fog as low-visibility conditions when visibility measured by the PWD22 sensor is reduced to less than 6 km (formally this is fog and mist). While both complexity of the coastal landforms and presence of tiny water droplets suspended in air (two-phase flow) violate assumptions underlying MOST, the non-dimensional standard deviations of the velocity components (especially φ_w) follow Monin–Obukhov predictions with surprisingly small scatter for foggy cases (Figs. 9 and 10). The data scatter for the normalized dissipation rate $\varphi_\varepsilon(\zeta)$ was somewhat greater as compared to the normalized standard deviations $\varphi_\alpha(\zeta)$.

A poor agreement of $\varphi_q(\zeta)$ with MOST was noted in the presence of fog, wherein the statistical dependence of $\varphi_q(\zeta)$ on the MOST stability parameter $\zeta = z/L$ was weak, if not non-existent (Fig. 12e, 12f). The measurements show a bias and relatively larger scatter of normalized standard deviations for scalars for $\varphi_\theta(\zeta)$ and $\varphi_q(\zeta)$ under near-neutral conditions, likely due to underlying costal surface that was inhomogeneous in temperature and moisture/water content. The larger scatter of data and poor correspondence of $\varphi_\theta(\zeta)$ and $\varphi_q(\zeta)$ with MOST in fog is possibly related to phase transition between liquid water and vapour. Evaporation of water droplets absorbs latent heat from environment and cools the surrounding air while condensation releases latent heat and warms the surrounding air, thus affecting σ_θ and σ_q. Thus, there is considerable room for improvements in future work, particularly with regard to the parameterization of sensible and latent heat fluxes and statistics of salient turbulence parameters from readily measured or modelled quantities.

Acknowledgements This research was funded by the Office of Naval Research (ONR) under the Award # N00014-18-1-2472 entitled: "Toward Improving Coastal Fog Prediction (C-FOG)". During the project, Dr. R. Krishnamurthy was partially funded by the Pacific Northwest National Laboratory (PNNL), which is operated by Battelle Memorial Institute for the Department of Energy (DOE) under Contract DE-AC05-76RL01830. We thank all who organized, deployed, operated, and maintained instrumentation that provided a valuable set of in situ measurements during the C-FOG field campaign. Their diligent and dedicated efforts are greatly appreciated. Finally, hats off to the townsfolk of Ferryland for their warm welcome, friendliness, and hospitality.

References

Bardoel SL, Horna Muñoz DV, Grachev AA, Krishnamurthy R, Chamorro LP, Fernando HJS (2021) Fog formation related to gravity currents interacting with coastal topography. Boundary-Layer Meteorol. https://doi.org/10.1007/s10546-021-00638-w

Burba G (2013) Eddy covariance method for scientific, industrial, agricultural and regulatory applications: A field book on measuring ecosystem gas exchange and areal emission rates. LI-COR Biosciences, Lincoln, USA, 331 pp. ISBN: 978-0-61576827-4

Carter R.W.G. (1988) Coastal environments. An introduction to the physical, ecological, and cultural systems of coastlines. Academic Press. 617 pp. https://doi.org/10.1016/C2009-0-21648-5

Dorman CE, Mejia J, Koračin D, McEvoy D (2017) Worldwide marine fog occurrence and climatology. In: Koračin D, Dorman CE (Eds.) Marine fog: Challenges and advancements in observations, modeling, and forecasting, Chapter 2. 7–152. Springer International Publishing Switzerland. https://doi.org/10.1007/978-3-319-45229-6_2

Dorman CE, Mejia J, Koračin D, McEvoy D (2020) World marine fog analysis based on 58-years of ship observations. Int J Climatol 40(1):145–168. https://doi.org/10.1002/joc.6200

Dorman CE, Hoch SW, Gultepe I, Fernando HJS, Krishnamurthy R (2021) Large scale synoptic systems and fog during the C-FOG field experiment. Boundary-Layer Meteorol (accepted)

Edson J, Crawford T, Crescenti J, Farrar T, Frew N, Gerbi G, Helmis C, Hristov T, Khelif D, Jessup A, Jonsson H, Li M, Mahrt L, McGillis W, Plueddemann A, Shen L, Skyllingstad E, Stanton T, Sullivan P, Sun J, Trowbridge J, Vickers D, Wang S, Wang Q, Weller R, Wilkin J, Williams AJ, Yue DKP, Zappa C (2007) The Coupled Boundary Layers and Air–Sea Transfer Experiment in Low Winds. Bull Amer Meteor Soc 88(3):341–356. https://doi.org/10.1175/BAMS-88-3-341

Emeis S (2014) Current issues in wind energy meteorology. Met Apps 21(4):803–819. https://doi.org/10.1002/met.1472

Fairall CW, Davidson KL, Houlihan TM, Schacher GE (1977) Atmospheric turbulence measurements in marine fog during CEWCOM-76. Naval Postgraduate School, Monterey, California 1977-12-29, NPS Report Number NPS61-77-004 (available at https://calhoun.nps.edu/handle/10945/29732)

Fairall CW, Bradley EF, Hare JE, Grachev AA, Edson JB (2003) Bulk parameterization of air-sea fluxes: updates and verification for the COARE algorithm. J Clim 16(4):571–591.

Fernando HJS, Gultepe I, Dorman C, Pardyjak E, Wang Q, Hoch SW, Richter D, Creegan E, Gaberšek S, Bullock T, Hocut C, Chang R, Alappattu D, Dimitrova R, Flagg D, Grachev A, Krishnamurthy R, Singh DK, Lozovatsky I, Nagare B, Sharma A, Wagh S, Wainwright C, Wroblewski M, Yamaguchi R, Bardoel S, Coppersmith RS, Chisholm N, Gonzalez E, Gunawardena N, Hyde O, Morrison T, Olson A, Perelet A, Perrie W, Wang S, Wauer B (2021) C-FOG: Life of coastal fog. Bull Amer Meteorol Society 102(2):E244–E272. https://doi.org/10.1175/BAMS-D-19-0070.1

Geernaert GL (2002) On extending the flux-profile similarity theory to include quasi-homogeneous conditions in the marine atmospheric surface layer. Boundary-Layer Meteorol 105(3):433–450. https://doi.org/10.1023/A:1020307703242

Golitsyn GS, Grachev AA (1986) Free convection of multi-component media and parameterization of air-sea interaction at light winds. Ocean-Air Interactions 1:57–78 (available at https://www.researchgate.net/publication/348728736_Free_convection_of_multi-component_media_and_parameterization_of_air-sea_interaction_at_light_winds)

Grachev AA, Bariteau L, Fairall CW, Hare JE, Helmig D, Hueber J, Lang EK (2011) Turbulent fluxes and transfer of trace gases from ship-based measurements during TexAQS 2006. J Geophys Res 116:D13110. https://doi.org/10.1029/2010JD015502

Grachev AA, Andreas EL, Fairall CW, Guest PS, Persson POG (2015) Similarity theory based on the Dougherty-Ozmidov length scale. Quart J Roy Meteorol Soc 141(690A):1845–1856. https://doi.org/10.1002/qj.2488

Grachev AA, Leo LS, Di Sabatino S, Fernando HJS, Pardyjak ER, Fairall CW (2016) Structure of turbulence in katabatic flows below and above the wind-speed maximum. Boundary-Layer Meteorol 159(3):469–494. https://doi.org/10.1007/s10546-015-0034-8

Grachev AA, Leo LS, Fernando HJS, Fairall CW, Creegan E, Blomquist BW, Christman AJ, Hocut CM (2018a) Air-sea/land interaction in the coastal zone. Boundary-Layer Meteorol 167(2):181–210. https://doi.org/10.1007/s10546-017-0326-2

Grachev AA, Persson POG, Uttal T, Akish EA, Cox CJ, Morris SM, Fairall CW, Stone RS, Lesins G, Makshtas AP, Repina IA (2018b) Seasonal and latitudinal variations of surface fluxes at two Arctic terrestrial sites. Clim Dyn 51(5-6):1793–1818. https://doi.org/10.1007/s00382-017-3983-4

Gultepe I, Tardif R, Michaelides S, Cermak J, Bott A, Bendix J, Müller MD, Pagowski M, Hansen B, Ellrod G, Jacobs W, Toth G, Cober SG (2007) Fog research: A review of past achievements and future perspectives. Pure Appl Geophys 164(6-7):1121–1159. https://doi.org/10.1007/s00024-007-0211-x

Gultepe I, Pearson G, Milbrandt JA, Hansen B, Platnick S, Taylor P, Gordon M, Oakley JP, Cober SG (2009) The Fog Remote Sensing and Modeling field project. Bull Amer Meteor Soc 90(3):341–360. https://doi.org/10.1175/2008BAMS2354.1

Gultepe I, Milbrandt JA, Zhou B (2017) Marine fog: A review on microphysics and visibility prediction. In: Koračin D, Dorman CE (Eds.) Marine fog: Challenges and advancements in observations, modeling, and forecasting, Chapter 7. 345–394. Springer International Publishing Switzerland. https://doi.org/10.1007/978-3-319-45229-6_7

Gultepe I, Pardyjak E, Hoch SW, Fernando HJS, Dorman C, Flagg DD, Krishnamurthy R, Wang Q, Gaberšek S, Creegan E, Scantland N, Desjardins S, Heidinger A, Pavolonis M, Heymsfield AJ (2021) Coastal fog microphysics using in-situ observations and GOES-R retrievals. Boundary-Layer Meteorol (accepted).

El-Madany TS, Griessbaum F, Fratini G, Juang J-Y, Chang S-C, Klemm O (2013) Comparison of sonic anemometer performance under foggy conditions. Agric For Meteorol 173:63-73. https://doi.org/10.1016/j.agrformet.2013.01.005

Heo KY, Ha KJ, Mahrt L, Shim J-S (2010) Comparison of advection and steam fogs: From direct observation over the sea. Atmos Res 98(2-4):426–437. doi:10.1016/j.atmosres.2010.08.004

ICAO (2007) Meteorological Service for International Air Navigation. Annex 3 to the convention on International Civil Aviation. International Civil Aviation Organization. Sixteenth Edition (available at https://www.wmo.int/pages/prog/www/ISS/Meetings/CT-MTDCF-ET-DRC_Geneva2008/Annex3_16ed.pdf)

Huang H, Liu H, Huang J, Mao W, Bi X (2015) Atmospheric boundary layer structure and turbulence during sea fog on the Southern China coast. Mon Wea Rev 143(5):1907–1923. https://doi.org/10.1175/MWR-D-14-00207.1

Lewis JM, Koračin D, Redmond KT (2004) Sea fog research in the United Kingdom and United States: A historical essay including outlook. Bull Amer Meteor Soc 85(3):395–408. https://doi.org/10.1175/BAMS-85-3-395

Kaimal JC, Finnigan JJ (1994) Atmospheric boundary layer flows: Their structure and measurements. Oxford University Press, New York and Oxford, 289 pp

Kim CK, Yum SS (2017) Turbulence in marine fog. In: Koračin D, Dorman CE (Eds) Marine fog: Challenges and advancements in observations, modeling, and forecasting, Chapter 4. 245–271. Springer International Publishing Switzerland. https://doi.org/10.1007/978-3-319-45229-6_4

Kljun N., Calanca P., Rotach, M.W., Schmid H.P. (2004) A simple parameterisation for flux footprint predictions. Boundary-Layer Meteorol 112(3): 503–523. https://doi.org/10.1023/B:BOUN.0000030653.71031.96

Kljun N, Calanca P, Rotach MW, Schmid HP (2015) A simple two-dimensional parameterisation for Flux Footprint Prediction (FFP). Geosci Model Dev 8:3695–3713. https://doi.org/10.5194/gmd-8-3695-2015

Koračin D., Dorman C.E., Lewis J.M., Hudson J.G., Wilcox E.M., Torregrosa A. (2014) Marine fog: A review. Atmos. Res. 143: 142–175. https://doi.org/10.1016/j.atmosres.2013.12.012

Koračin D, Dorman CE (2017) Marine fog: challenges and advancements in observations, modeling, and forecasting. Koračin D, Dorman CE (Eds), Springer International Publishing Switzerland. 537 p. https://doi.org/10.1007/978-3-319-45229-6

Mahrt L, Vickers D, Edson J, Sun J, Højstrup J, Hare J, Wilczak JM (1998) Heat flux in the coastal zone. Boundary-Layer Meteorol 86(3):421–446. DOI: 10.1023/A:1000784219817

Mahrt L, Andreas EL, Edson JB, Vickers D, Sun J, Patton EG (2016) Coastal zone surface stress with stable stratification. J Phys Oceanogr 46(1):95–105. DOI: 10.1175/JPO-D-15-0116.1

Mahrt L, Thomas CK, Grachev A, Persson POG (2018) Near-surface vertical flux divergence in the stable boundary layer. Boundary-Layer Meteorol 169(3): 373–393. https://doi.org/10.1007/s10546-018-0379-x

Leclerc MY, Foken T (2014) Footprints in micrometeorology and ecology. Springer-Verlag Berlin Heidelberg, 239 pp. https://doi.org/10.1007/978-3-642-54545-0

Obukhov AM (1946) Turbulence in an atmosphere with a non-uniform temperature. Trudy Inst Teoret Geofiz Akad Nauk SSSR 1:95–115 (translation in: Boundary-Layer Meteorol 1971 2:7–29)

Ortiz-Suslow DG, Haus BK, Williams NJ, Laxague NJM, Reniers AJHM, Graber HC (2015) The spatial-temporal variability of air-sea momentum fluxes observed at a tidal inlet. J Geophys Res Oceans 120(2):660–676. https://doi.org/10.1002/2014JC010412

Ortiz-Suslow DG, Haus BK, Williams NJ, Graber HC, MacMahan JH (2018) Observations of air-sea momentum flux variability across the inner shelf. J Geophys Res Oceans 123(12):8970–8993. https://doi.org/10.1029/2018JC014348

Ortiz-Suslow DG, Kalogiros J, Yamaguchi R, Alappattu D, Franklin K, Wauer B, Wang Q (2019) The data processing and quality control of the marine atmospheric boundary layer measurement systems deployed by the Naval Postgraduate School during the CASPER-West field campaign. Naval Postgraduate School, Monterey, California 2019-03, NPS Report Number NPS-MR-19-001 v1.1, 98 pp. (available at https://calhoun.nps.edu/handle/10945/61638)

Ortiz-Suslow DG, Wang Q, Kalogiros J, Yamaguchi R (2020) A method for identifying kolmogorov's inertial subrange in the velocity variance spectrum. J Atmos Ocean Technol 37(1):85-102. https://doi.org/10.1175/JTECH-D-19-0028.1

Perelet AO, Gultepe I, Hoch SW, Pardyjak ER (2021) Discriminating fog and rain at the kilometre scale using the extinction from collocated infrared and microwave scintillometers. Boundary-Layer Meteorol. https://doi.org/10.1007/s10546-021-00609-1

Saunders PM (1964) Sea smoke and steam fog. Quart J Roy Meteorol Soc 90(384): 56–165. https://doi.org/10.1002/qj.49709038405

Siebert H, Teichmann U (2000) Behaviour of an ultrasonic anemometer under cloudy conditions. Boundary-Layer Meteorol 94(1):165-169. https://doi.org/10.1023/A:1002446723575

Sun J, Vandemark D, Mahrt L, Vickers D, Crawford T, Vogel C (2001) Momentum transfer over the coastal zone. J Geophys Res 106(D12):12437–12448. https://doi.org/10.1029/2000JD900696.

Torregrosa A, O'Brien TA, Faloona IC (2014) Coastal fog, climate change, and the environment. Eos Trans AGU 95(50):473–484. https://doi.org/10.1002/2014EO500001

Vautard R, Yiou P, Van Oldenborgh GJ (2009) Decline of fog, mist and haze in Europe over the past 30 years. Nature Geosci 2(2):115–119. https://doi.org/10.1038/ngeo414

Vickers D, Mahrt L (1997) Quality control and flux sampling problems for tower and aircraft data. J Atmos Oceanic Technol 14(3):512–526

Wang Q, Alappattu DP, Billingsley S, Blomquist B, Burkholder RJ, Christman AJ, Creegan ED, de Paolo T,. Eleuterio DP, Fernando HJS, Franklin KB, Grachev AA, Haack T, Hanley TR, Hocut CM, Holt TR, Horgan K, Jonsson HH, Hale RA, Kalogiros JA, Khelif D, Leo LS, Lind RJ, Lozovatsky I, Panella-Morato J, Mukherjee S, Nuss WA, Pozderac J, Rogers LT, Savelyev I, Savige DK, Shearman RK, Shen L, Terrill E, Ulate AM, Wang Q, Wendt RT, Wiss R, Woods RK, Xu L, Yamaguchi RT, Yardim C (2018) CASPER: Coupled Air-Sea Processes and Electromagnetic (EM) Wave ducting Research. Bull Amer Meteorol Society 99(7):1449–1471. https://doi.org/10.1175/BAMS-D-16-0046.1

Wang B (1985) Sea fog. China Ocean Press, Beijing. 330p

Watton EC (2016) Coastal geomorphology, processes and erosion at the tourist destination of Ferryland, Newfoundland and Labrador. M.Sc. thesis, Memorial University of Newfoundland, St. John's, 213 p

Webb EK, Pearman GI, Leuning R (1980) Correction of flux measurements for density effects due to heat and water vapour transfer. Quart J Roy Meteorol Soc 106(447):85–100. https://doi.org/10.1002/qj.49710644707

Fig. 1 Topography of the Study Area (Department of Energy, Mines, and Resources Canada, "Ferryland" map, 1984.). The position of the UND flux tower at The Downs (47°01'17.1"N and 52°52'19.5"W) is shown as a yellow star. Grid lines are 1000 m apart. See also Watton (2016, Fig. 1.3) for further detail

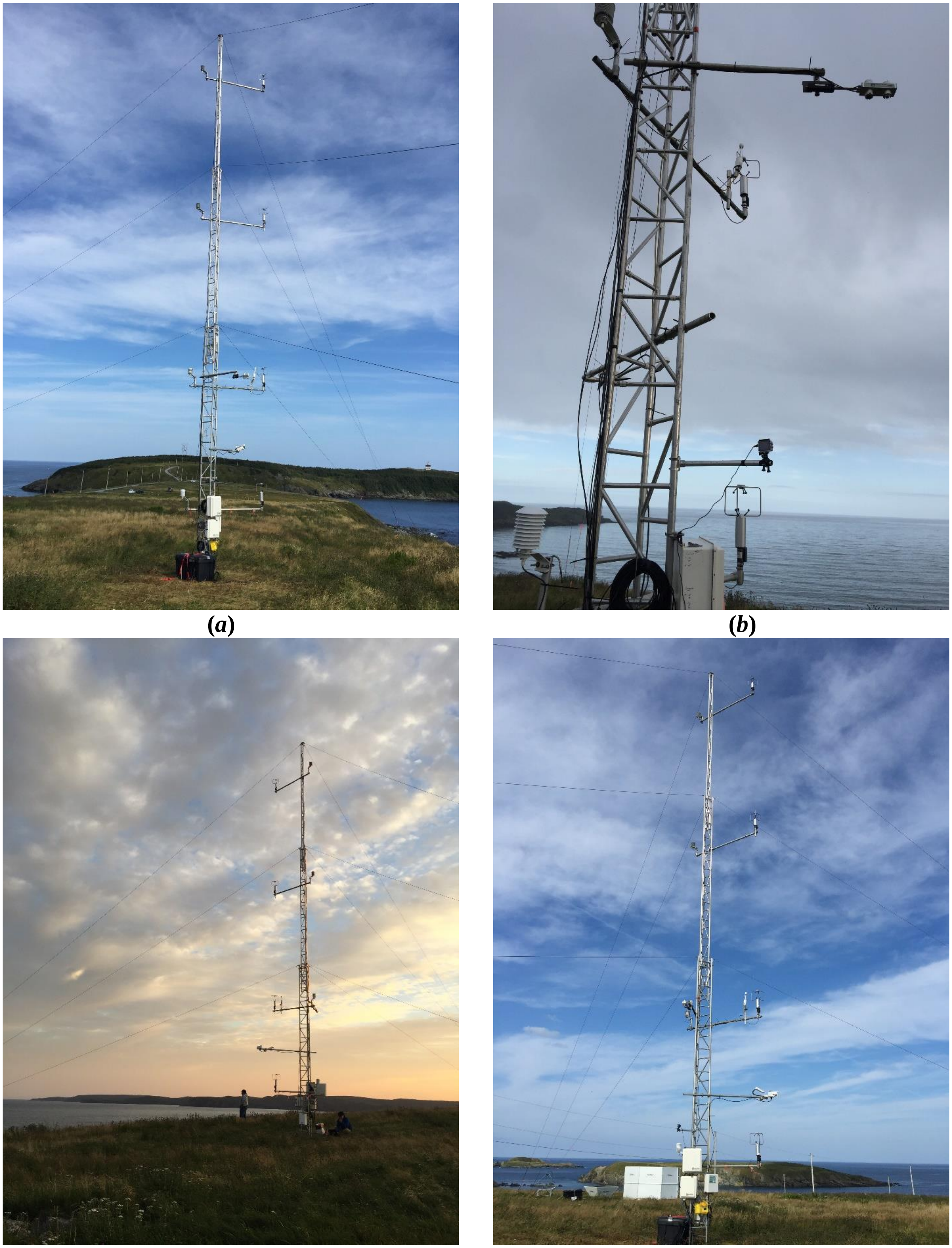

(***a***) (***b***) (***c***) (***d***)

Fig. 2 View of the UND flux tower and instruments looking toward (*a*) east (Ferryland Head Lighthouse), (*b*) south-east, (*c*) south-west, and (*d*) north (Bois Island) during the C-FOG 2018 field campaign. Photos were taken (*a*) 3 September at 1612 NDT, (*b*) 2 September at 1806 NDT, (*c*) 24 August at 1941 NDT, and (*d*) 3 September at 1614 NDT by Andrey Grachev

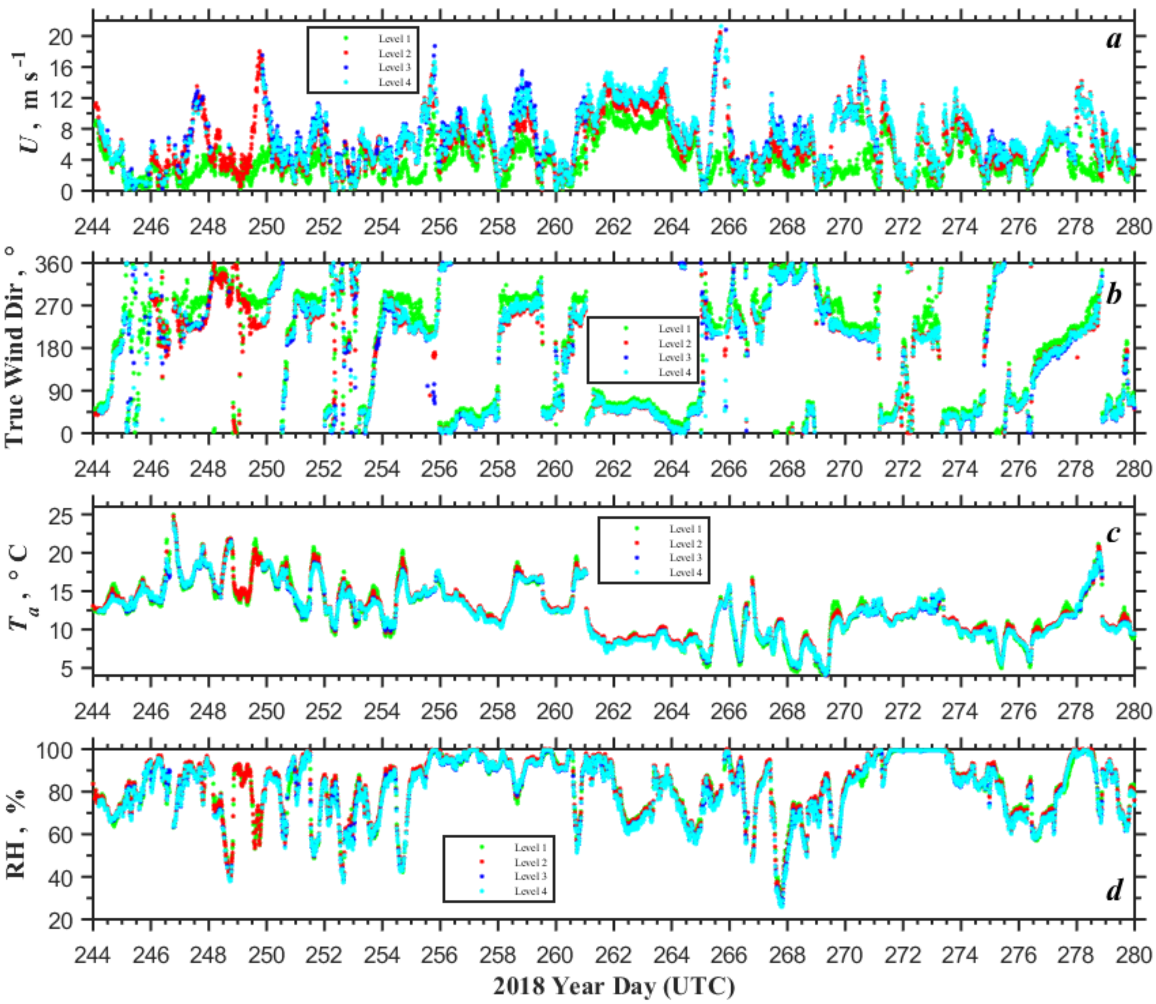

Fig. 3 Time series of (*a*) wind speed, (*b*) true wind direction, (*c*) air temperature, and (*d*) relative humidity for year days from 244 through 279 (from 1 September through 6 October 2018) observed at four levels of the UND flux tower located at The Downs measurement site in Ferryland, Newfoundland. The data are based on 15-min averaging

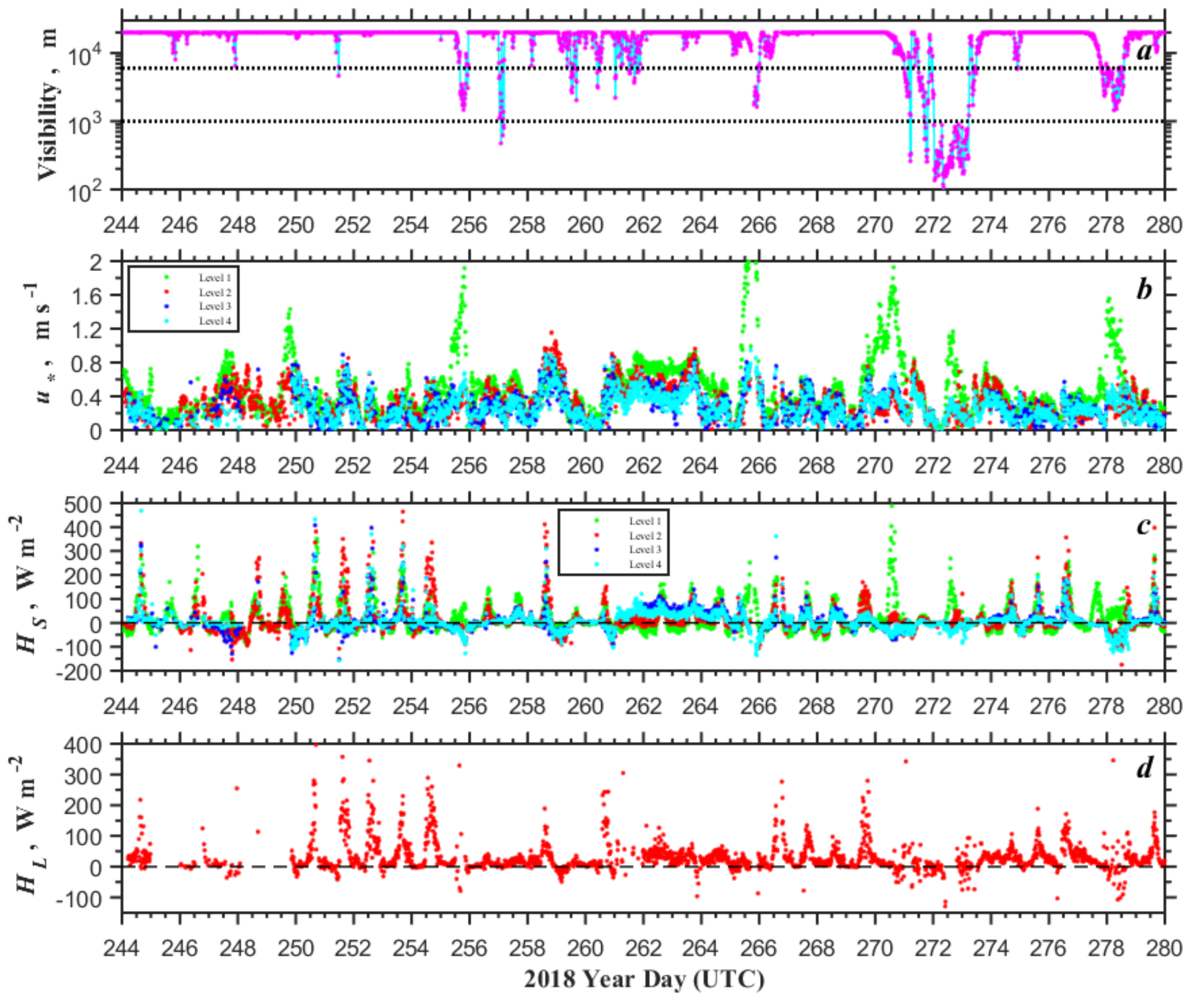

Fig. 4 Time series of (*a*) visibility, (*b*) friction velocity, u_*, (*c*) sensible heat flux, H_S, and (*d*) latent heat (water vapour) flux, H_L, for year days from 244 through 279 (from 1 September through 6 October 2018) observed at Ferryland, Newfoundland (the UND flux tower at The Downs measurement site). The data are based on 15-min averaging. The sign convention for sensible heat flux generally indicates a SBL when $H_S < 0$ and a CBL when $H_S > 0$. Horizontal dotted lines in panel (*a*) mark the visibility thresholds for fog (visibility < 1 km) and mist (1–6 km)

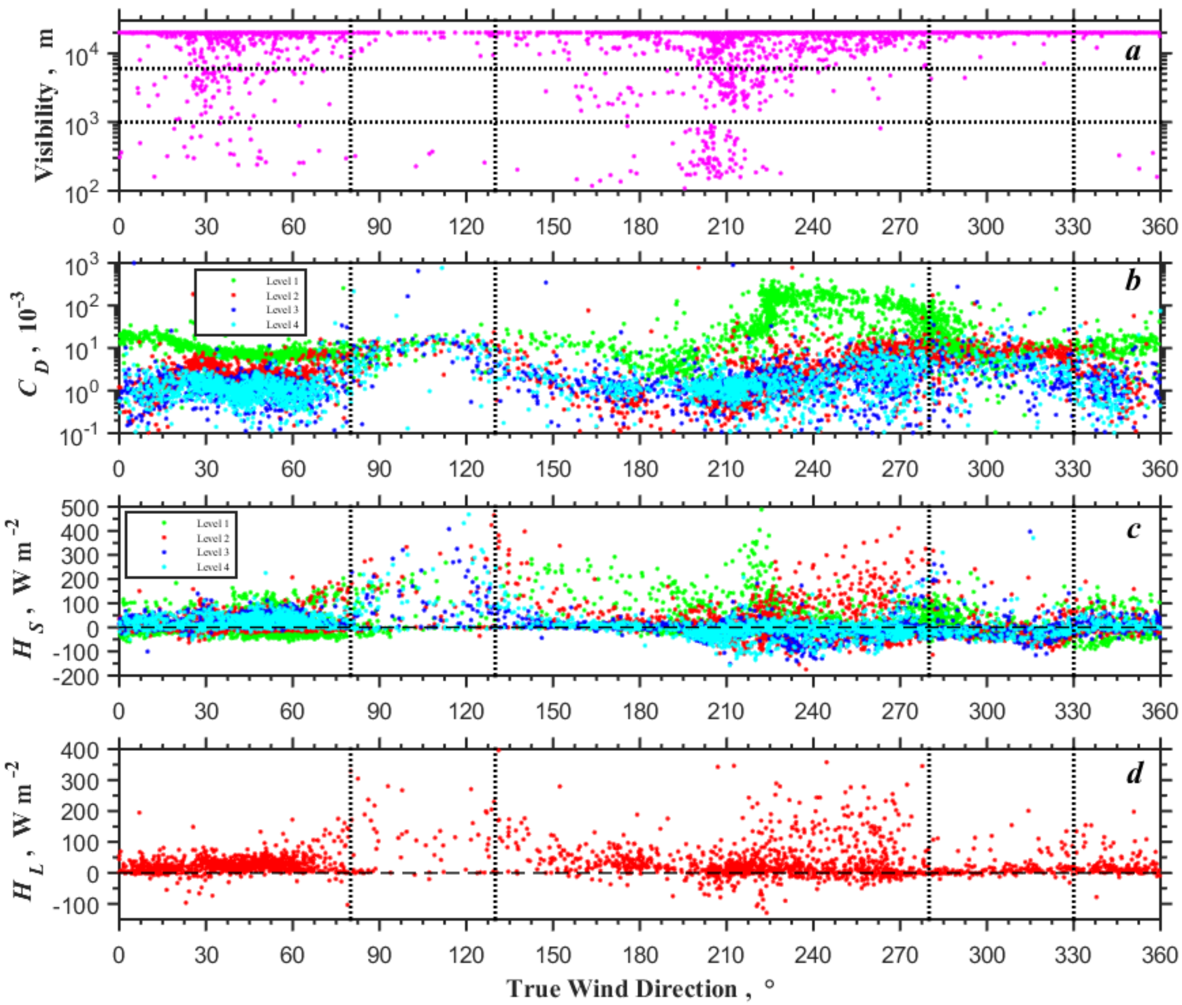

Fig. 5 Individual 15-min-averaged data of the(*a*) visibility, (*b*) drag coefficient, $C_D = (u_*/U)^2$, (*c*) sensible heat flux, H_S, and (*d*) latent heat (water vapour) flux, H_L, plotted versus the true wind direction for the data collected at the UND flux tower at The Downs/Ferryland measurement site during 1 September–6 October 2018 (year days 244–279). Horizontal dotted lines in panel (*a*) mark the visibility thresholds for fog (visibility < 1 km) and mist (1–6 km). Vertical dotted lines indicate wind sectors when local wind blows approximately along The Downs land formation (Fig. 1); i.e., the sector between ≈ 80° and ≈ 130° (easterly winds) and in the sector between ≈ 280° and ≈ 330° (westerly winds)

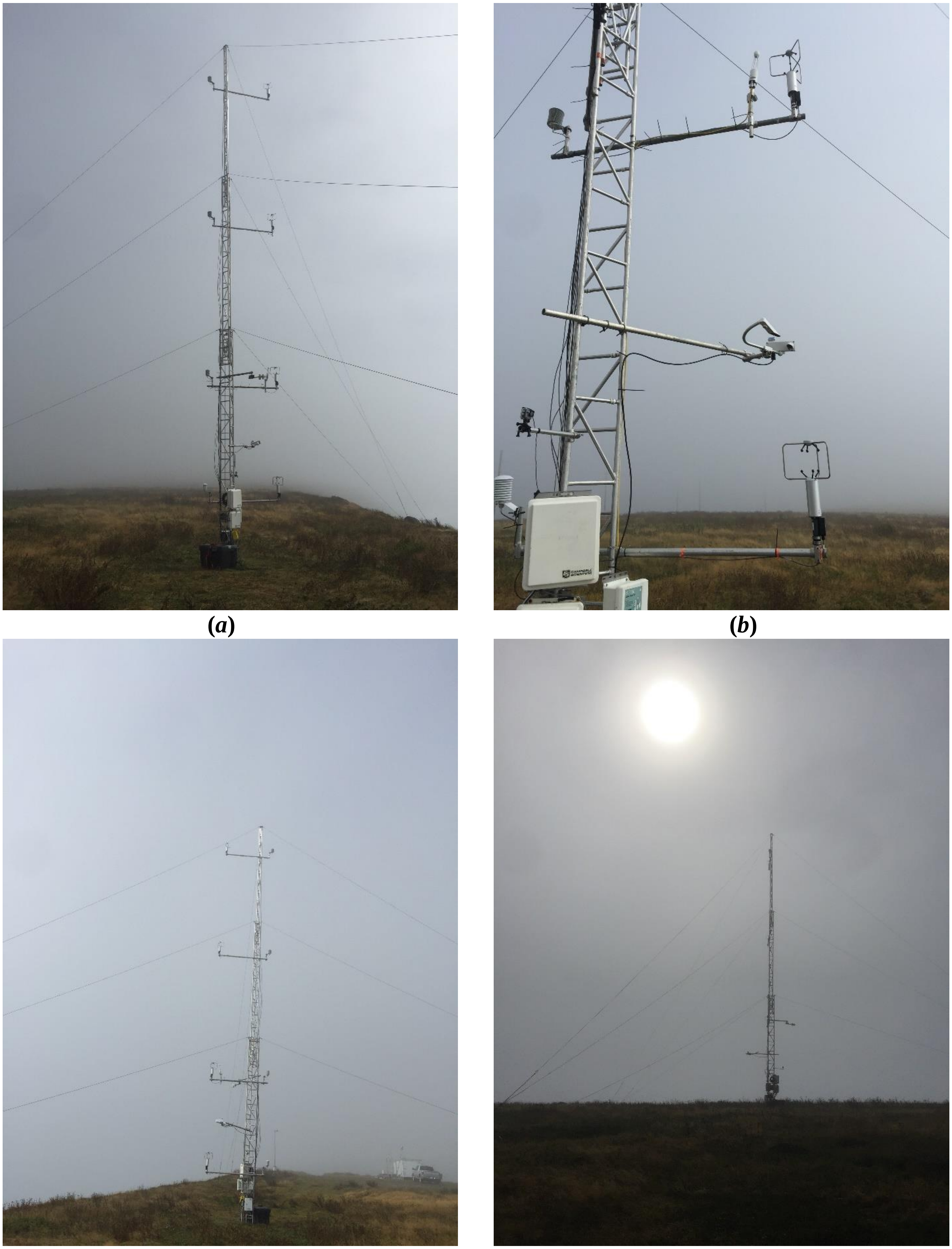

Fig. 6 View of the UND flux tower and instruments looking toward (*a*) east (Ferryland Head Lighthouse), (*b*) north-east, (*c*) west-south-west (Town of Ferryland), and (*d*) south during a fog event. Photos were taken during the long IOP-10 on 29 September 2018 (year day 272) at *a*) 1141 NDT, (*b*) 1200 NDT, (*c*) 1143 NDT, and (*d*) 1139 NDT. Photos credit: Andrey Grachev

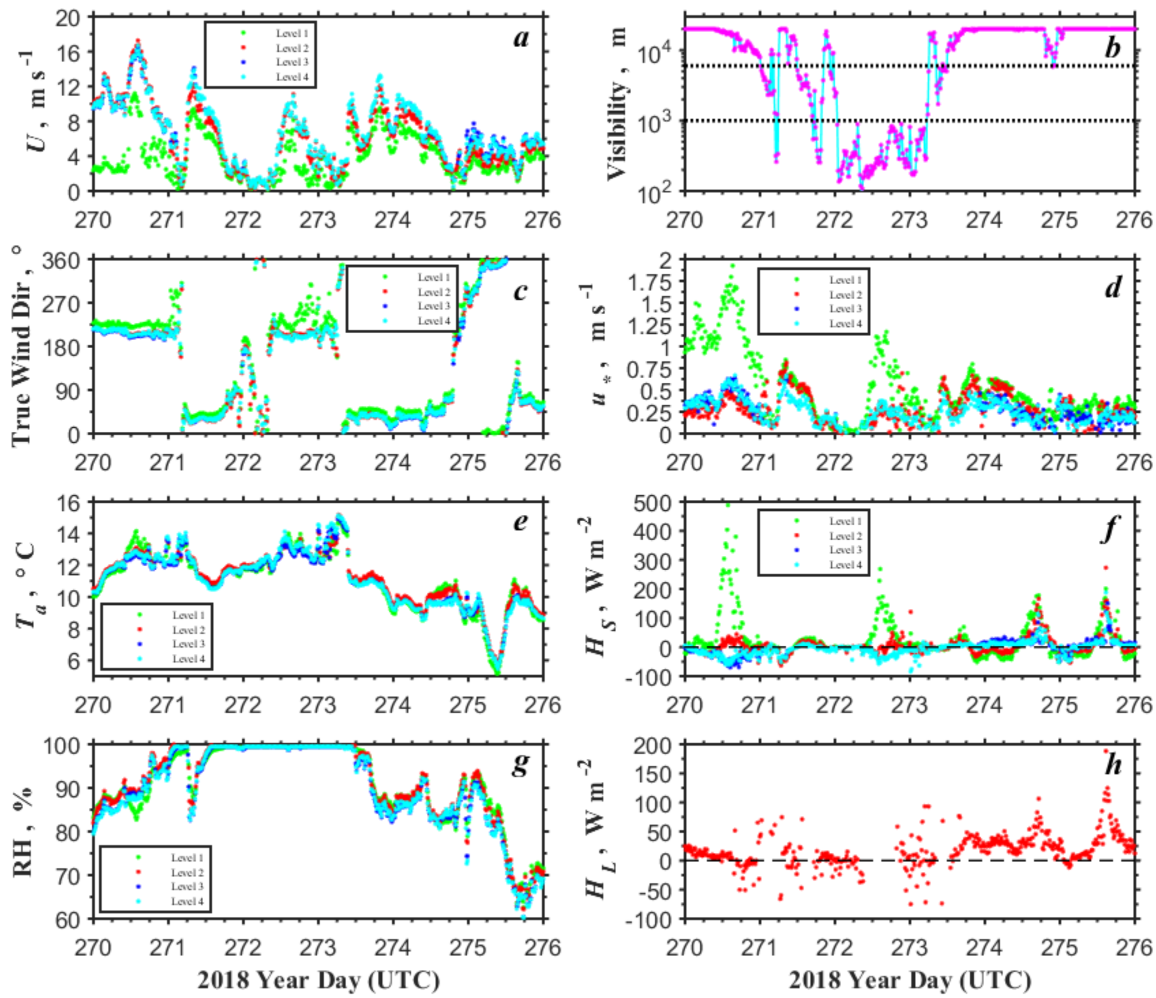

Fig. 7 Time series of (*a*) wind speed, (*b*) visibility, (*c*) true wind direction, (*d*) friction velocity, u_*, (*e*) air temperature, (*f*) sensible heat flux, H_S, (*g*) relative humidity, and (*h*) latent heat (water vapour) flux, H_L, for year days from 270 to 276 (from 27 September to 3 October 2018) including the long IOP-10 (year days 270–273) observed at the UND flux tower (Ferryland/Downs site). The data are based on 15-min averaging. Horizontal dotted lines in panel (*b*) mark the visibility thresholds for fog (visibility < 1 km) and mist (1–6 km)

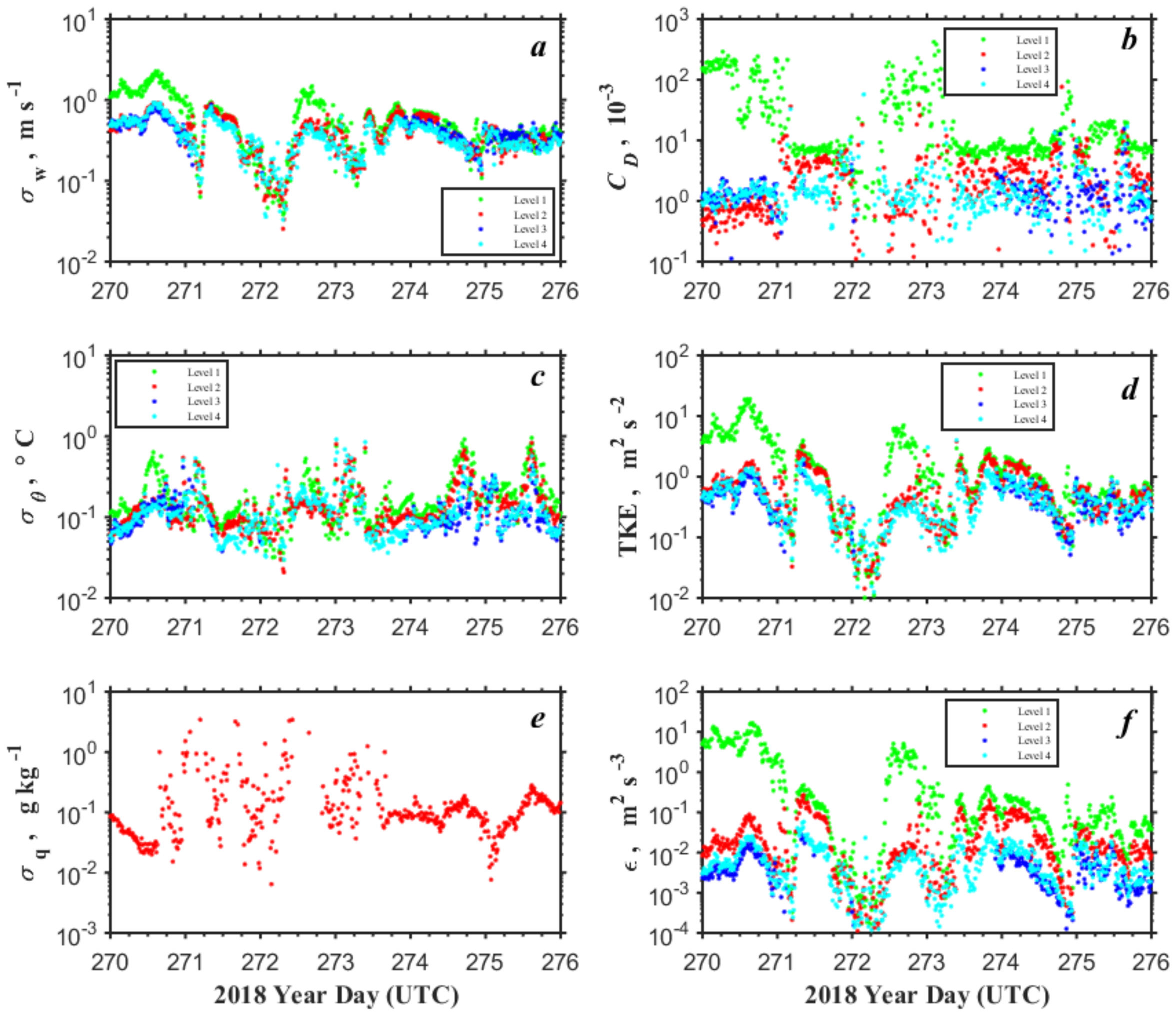

Fig. 8 Same as Fig. 7 but for time series of (*a*) standard deviation of the vertical velocity component, σ_w, (*b*) drag coefficient, C_D, (*c*) standard deviation of the sonic temperature, σ_θ, (*d*) TKE, (*e*) standard deviation of the specific humidity, σ_q, and (*f*) dissipation rate of the TKE, ε

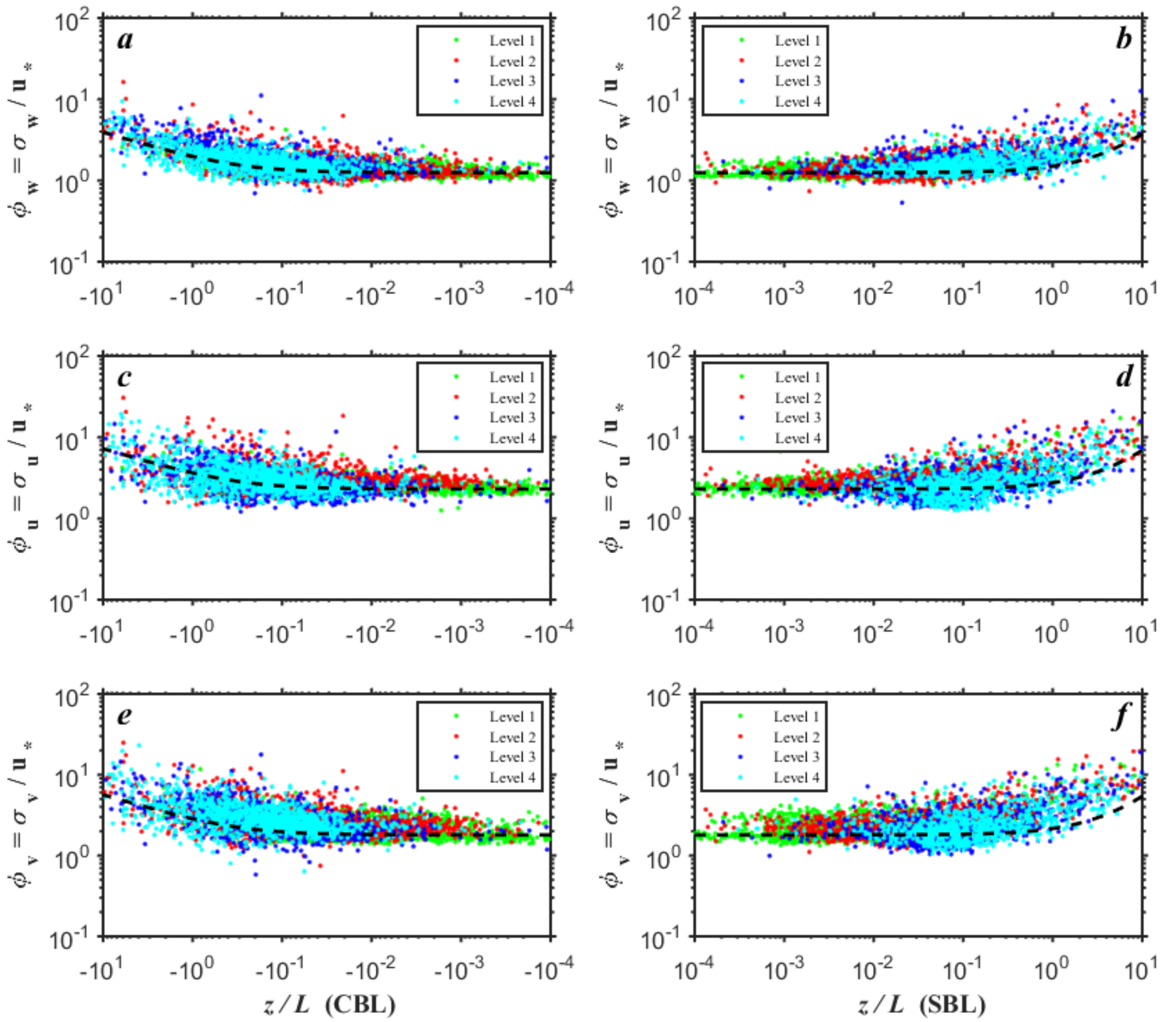

Fig. 9 The non-dimensional standard deviations of the (*a*, *b*) vertical, (*c*, *d*) longitudinal, and (*e*, *f*) lateral velocity components (6) plotted in log-log coordinates versus the local Monin–Obukhov stability parameter (5) for the 15-min-averaged data collected during only clear sky days with high visibility (i.e., fog-free conditions) when the PWD22 visibility was greater than 6 km. Plots in the left panels (*a*, *c*, *e*) correspond to unstable conditions, or CBL, $\zeta < 0$; the right panels (*b*, *d*, *f*) represent stable conditions, or SBL, $\zeta > 0$. The black dashed lines correspond to $\varphi_\alpha(\zeta) = c_\alpha(1-3\zeta)^{1/3}$ for $\zeta < 0$ and $\varphi_\alpha(\zeta) = c_\alpha(1+0.2\zeta)$ for $\zeta > 0$ where α (= *u*, *v*, and *w*) and $c_u = 2.3$, $c_v = 1.8$, $c_w = 1.25$ (Kaimal and Finnigan 1994)

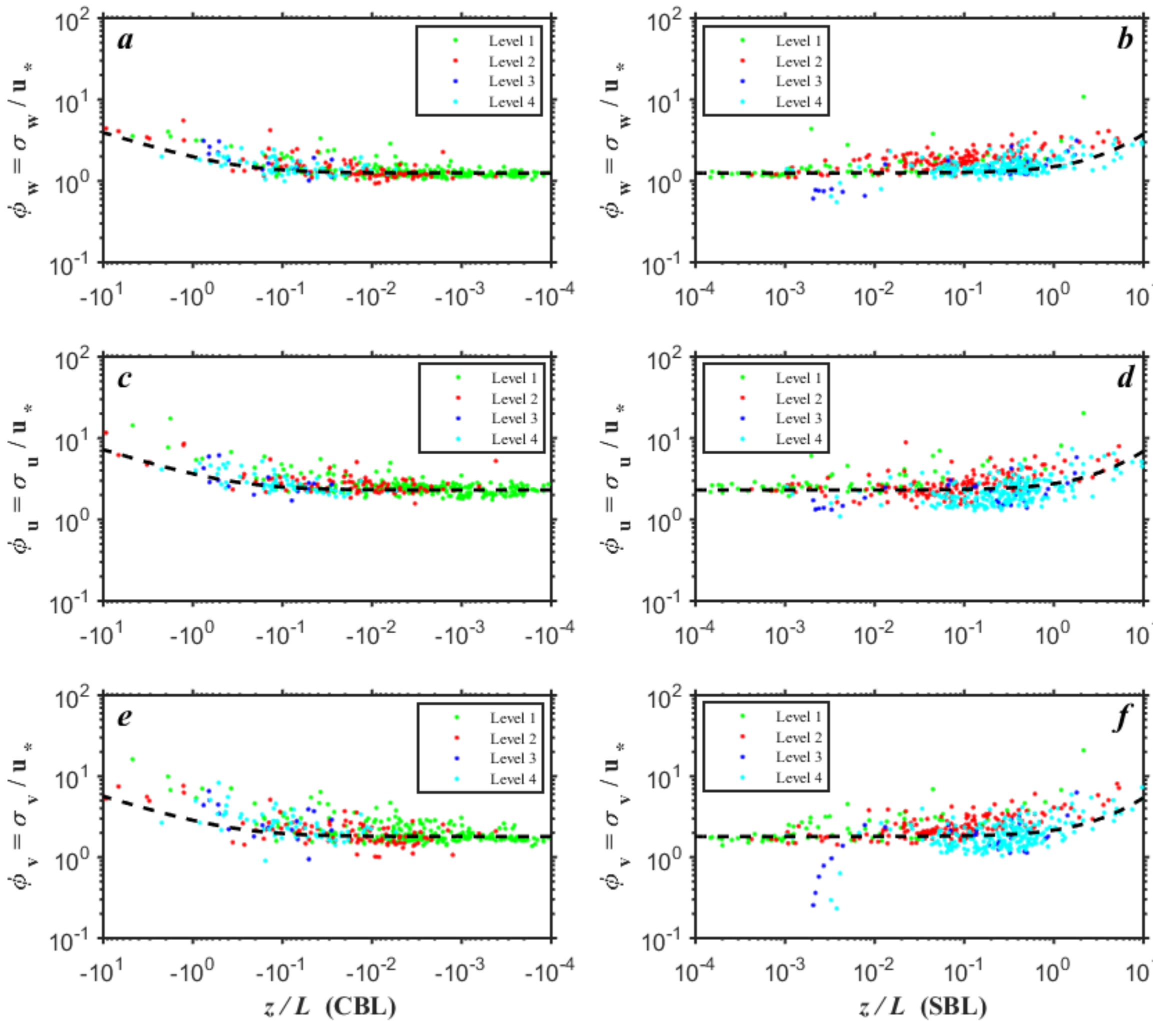

Fig. 10 Same as Fig. 9 but for low-visibility conditions (fog and mist) when the PWD22 visibility was less than 6 km

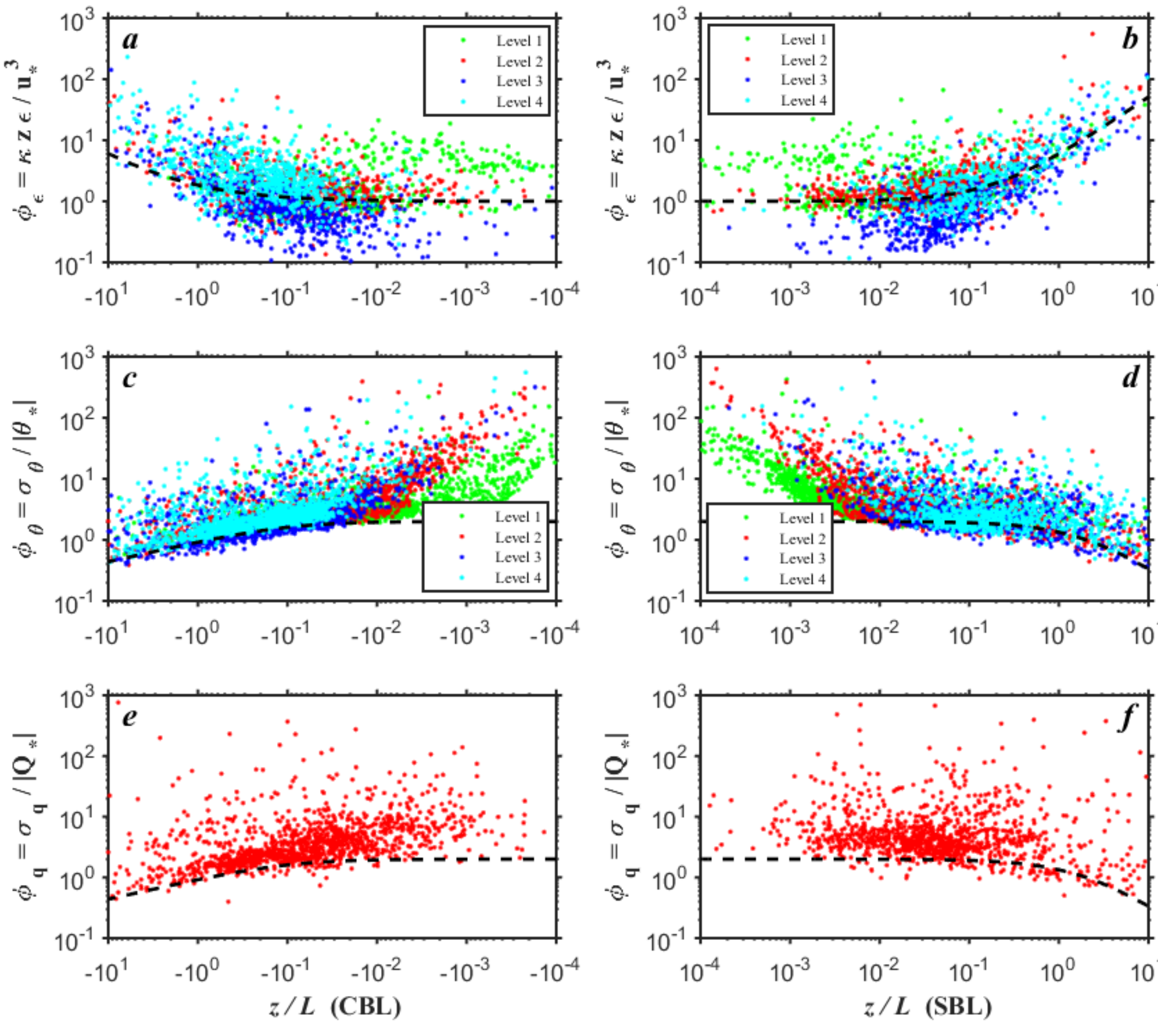

Fig. 11 The non-dimensional (*a*, *b*) dissipation rate of TKE (9), and standard deviations of the (*c*, *d*) air temperature (7), and (*e*, *f*) specific humidity (8) plotted in log-log coordinates versus the local Monin–Obukhov stability parameter (5) for the 15-min-averaged data collected during only clear sky days with high visibility (i.e., fog-free conditions) when the PWD22 visibility was greater than 6 km. Plots in the left panels (*a*, *c*, *e*) correspond to unstable conditions, or CBL, $\zeta < 0$; the right panels (*b*, *d*, *f*) represent stable conditions, or SBL, $\zeta > 0$. The black dashed lines correspond to $\varphi_\varepsilon(\zeta) = \left(1 + 0.5|\zeta|^{2/3}\right)^{1/3}$ for $\zeta < 0$ and $\varphi_\varepsilon(\zeta) = (1 + 5\zeta)$ for $\zeta > 0$; and $\varphi_\theta(\zeta) = \varphi_q(\zeta) = 2(1 - 9.5\zeta)^{1/3}$ for $\zeta < 0$ and $\varphi_\theta(\zeta) = \varphi_q(\zeta) = 2(1 + 0.5\zeta)$ for $\zeta > 0$ (Kaimal and Finnigan 1994)

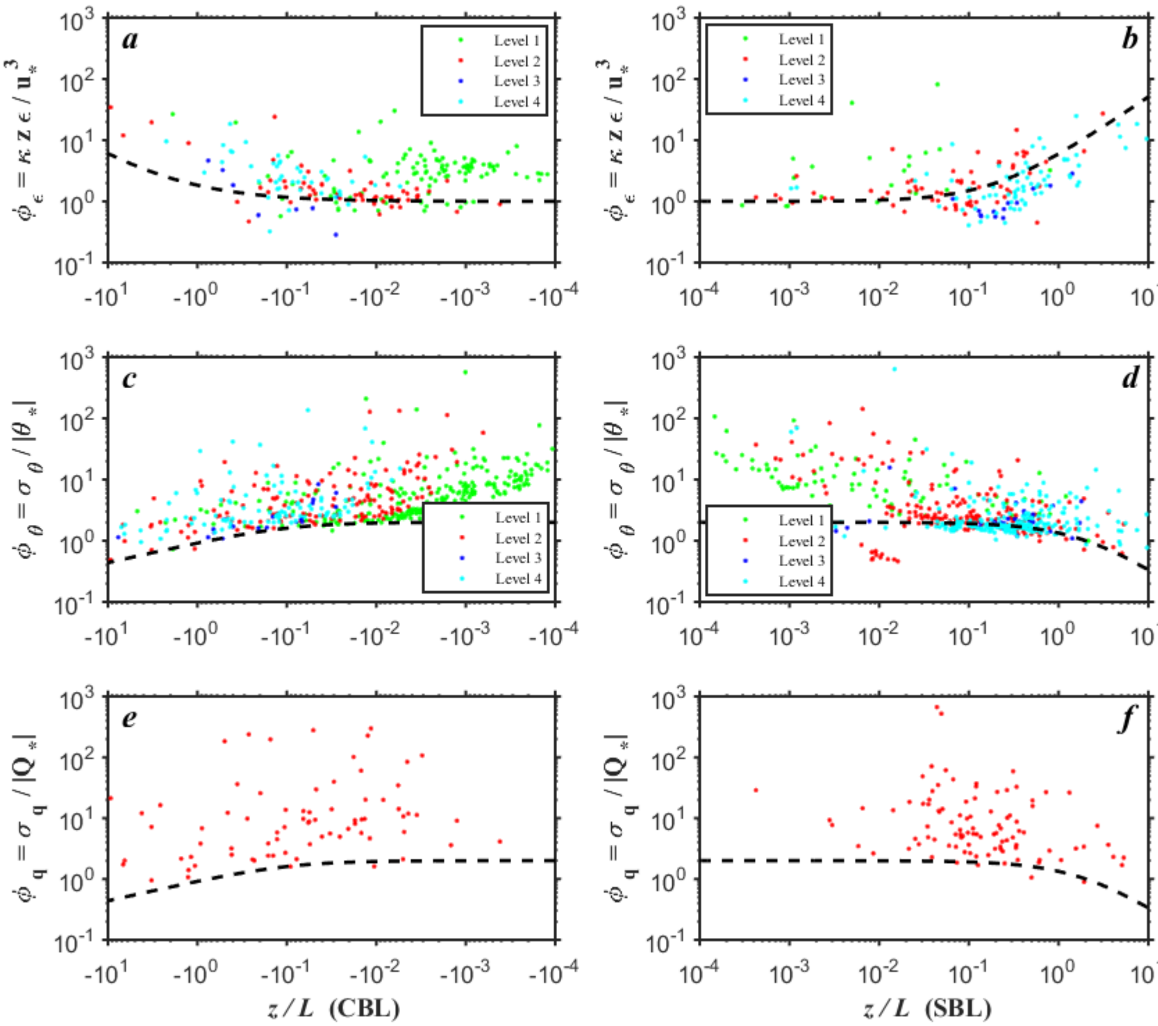

Fig. 12 Same as Fig. 11 but for low-visibility conditions (fog and mist) when the PWD22 visibility was less than 6 km